Atomistic simulations of the magnetic properties of Ir$_x$Mn$_{1-x}$ alloys

Sarah Jenkins ◉,[*] Roy. W. Chantrell ◉, and Richard F. L. Evans ◉[†]

Department of Physics, University of York, York, YO10 5DD, United Kingdom

Iridium manganese (IrMn) is arguably the most important antiferromagnetic material for device applications due to its metallic nature, high Néel temperature, and exceptionally high magnetocrystalline anisotropy. Despite its importance, its magnetic properties are poorly understood due to its intrinsic complexity and the interplay between structural and magnetic properties. Here we present a unifying atomistic model of Ir$_x$Mn$_{(1-x)}$ alloys which reproduces the key experimental facts of the material, while providing unprecedented understanding of the compositional and structural origins of its magnetic ground state and thermodynamic properties. We find that the Néel temperature is strongly dependent on the nature of the ground-state magnetic order which varies with x from a triangular to tetrahedral spin structure, leading to different levels of geometric spin frustration. The Néel temperature increases linearly with manganese concentration for the disordered phase, while the ordered phases show a peak for Ir$_{50}$Mn$_{50}$ followed by a decrease due to increased spin frustration. The ground-state tetrahedral spin structure of the disordered phase is composition independent for manganese concentrations in the 50–95% range, while the degree of spin order varies strongly in the same range. For low manganese concentrations, we find antiferromagnetic spin-glass and ferromagnetic ground-state spin structures. The magnetic anisotropy energy exhibits a complex dependence on the lattice symmetry, presenting easy-plane, cubic, and unconventional symmetries for the principal phases, and a similarly complex variation of magnitude. The complexity of behavior represents a dual blessing and a curse in that the properties of a particular sample depend strongly on the degree of order and composition, while also providing a large state space to engineer an antiferromagnet with optimal symmetry, magnetic anisotropy, and thermal stability. Such effects are important for the future development of nanoscale sensor devices and antiferromagnetic spintronics.

DOI: 10.1103/PhysRevMaterials.5.034406

I. INTRODUCTION

In his 1970 Nobel lecture, Louis Néel stated, "Antiferromagnetic materials are extremely interesting from the theoretical viewpoint, but do not seem to have any practical application" [1]. Since then, antiferromagnetic (AFM) materials have become a key feature in nearly all magnetic recording technologies and more recently have become an area of great research interest due to the development of AFM spintronic devices. AFM spintronics uses the AFM as the active element to store, read, or write information, in contrast to conventional spintronic devices which use ferromagnets (FMs) as the active element. AFM spintronics has the potential for very high data density as the elements can be tightly packed due to the lack of stray fields eliminating cross talk between neighboring devices [2]. The write times could be 1000 times faster [3] than conventional spintronic devices due to the THz timescales of the AFM spin dynamics. The magnetization is also exceptionally robust, as they are impervious to external magnetic fields. Their robust nature, however, comes at a price: their magnetization is notoriously difficult to manipulate. One possibility comes from coupling the AFM to a FM, as is done in giant magnetoresistive (GMR) sensors. Usually,

in these sensors the AFM is assumed to be approximately fixed. However if the AFM has a weak anisotropy, when the external magnetic field reorients the FM the AFM can be reoriented as well, controlling the motion of the AFM [4,5]. The current challenge in the development of AFM spintronic devices is a full understanding of the AFM properties such as basic characterization, the exact spin structures, and the size and symmetry of the magnetic anisotropies [6].

FM materials have been extensively investigated both experimentally and theoretically. AFM materials, though naturally much more abundant, were only discovered in the 1930s due to their lack of macroscopic stray fields. AFM materials lack macroscopic stray fields due to the exchange interactions ($\mathscr{H}_{ex}$), defined between pairs of neighboring spins,

$$\mathscr{H}_{ex} = -J_{ij}(\mathbf{S}_i \cdot \mathbf{S}_j) = -J_{ij}\cos(\theta), \qquad (1)$$

where J_{ij} is the exchange constant and $\mathbf{S}$ is the spin vector of two spins i and j. In FM materials, the minimum energy occurs when the spins ($\mathbf{S}_i$ and $\mathbf{S}_j$) align parallel, whereas in AFM materials the minimum energy occurs when the spins align antiparallel, causing the magnetizations to cancel out, giving no stray fields. Ideally, the magnetization of atoms in neighboring sublattices would lie 180° apart. In collinear AFMs, this is the case and there is no frustration of the spin structure. This is the case for a two-sublattice AFM, where the sublattices

─────────

[*]sarah.jenkins@york.ac.uk

[†]richard.evans@york.ac.uk
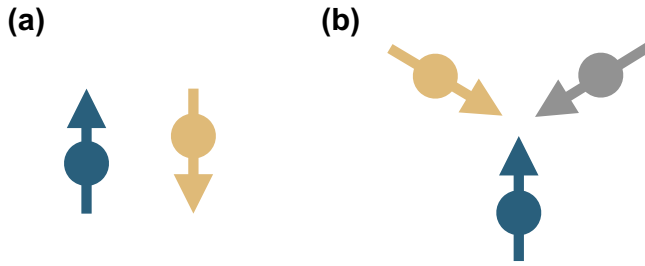
(a)   **(b)**

FIG. 1. Magnetic spin structures for antiferromagnetic materials with (a) two sublattices and (b) three sublattices. (a) The antiferromagnetic with two sublattices has a collinear magnetic structure (b) three sublattices has a noncollinear three sublattice magnetic structure.

are oriented antiparallel as shown in Fig. 1(a). However, for AFMs with more than two sublattices, the situation is much more subtle as the sublattices cannot all orient antiparallel. Instead, a much more complex frustrated spin structure is found. For three sublattices, the magnetization often forms a triangular spin structure known as the 3Q spin structure with the three sublattices making an angle of $120°$ with each other, as shown in Fig. 1(b). Although this is a minimum energy state, there is a degree of frustration in the spin structure as the atomic spins are oriented at $120°$ rather than $180°$. As the number of sublattices increases, the complexity of the spin structures increases leading to increased frustration.

In AFM materials, the internal magnetic moments exhibit flux closure, producing minimal detectable fields around the bulk material [7]. The lack of a bulk magnetization means that some of the magnetic properties such as Néel temperature or magnetic ground states are much harder to determine experimentally, especially in more complex noncollinear AFMs or in thin-film devices. The recent interest in AFMs for spintronic applications has led to many experimental developments in an attempt to probe the spin structures, such as using optical approaches [8] and investigating spin transport effects [9,10]. However, our knowledge of AFMs still lacks basic understanding and remains a complex and interesting challenge [2]. The AFM most widely used in spintronic devices is iridium manganese (IrMn) due to its high magnetic ordering temperature and high magnetic anisotropy. Iridium manganese has a very complex structure as, depending on the order and composition of the Ir and Mn concentrations, the number of sublattices and magnetic ground state changes. This means that previously there has been a lot of confusion around the magnetic spin structures of IrMn. Due to the problems in experimentally probing the magnetic structure of an AFM material, very few measurements exist. Experimental measurements of IrMn were done in 1973 by Yamaoka *et al.* [11]. They used neutron diffraction to look at the γ phases of $Ir_{1-x}Mn_x$ alloys with $x = 0.128$, 0.17, 0.204, and 0.256. They found that increasing the Ir concentration slightly increased the Néel temperature. In 1999, Tomeno *et al.* [12] used neutron diffraction to study a single crystal of $L1_2$-ordered $IrMn_3$. They found an exceptionally high magnetic ordering temperature of 960 K and a triangular (T1) spin structure. In 2013, Kohn *et al.* [13] determined the magnetic structures of single-crystal thin films of $IrMn_3$ in both the

fully ordered $L1_2$ phase and the fully disordered γ phase. They found a high Néel temperature for $IrMn_3$ of around 730 K for the γ phase and 1000 K for the $L1_2$ phase, respectively. They also determined the ground-state spin structure for both species using crystal neutron diffraction. For chemically ordered $L1_2$-$IrMn_3$ epitaxial thin films, they found the T1 magnetic structure with threefold symmetry that was previously reported for bulk $IrMn_3$. In the case of chemically disordered γ-$IrMn_3$, they found a cubic symmetry in which moments are tilted away by $45°$ from crystal diagonals toward the cube faces. Due to the complex anisotropy of IrMn, atomistic models have previously proved impossible and the spin structures have previously only been found using *ab initio* methods. Sakuma *et al.* [14] used the tight-binding linear muffin tin orbital method based on the local spin density functional approximation to calculate the magnetic structure of disordered $Mn_{100-x}Ir_x$ alloys and ordered $IrMn_3$ alloy. The disordered γ-$IrMn_3$ phase showed the 3Q structure as observed by Kohn *et al.* They found that the 3Q structure remained until x was less than 13, then the structure became the 2Q structure. For the ordered $L1_2$ system, they found the T1 ground state as found by Tomeno *et al.* [12]. Szunyogh *et al.* [15] calculated the magnetic properties of ordered IrMn and $IrMn_3$. They found that both IrMn phases had extremely high magnetic ordering temperatures of 1360 K and 1005 K, respectively. They found that for the ground state of ordered IrMn, the Mn atoms align along the [110] directions, indicating a collinear two-sublattice AFM with easy plane anisotropy. For the ordered $L1_2$ system, they again found the T1 ground state.

Due to the complexity of the material, incorrect assumptions have often been made in the literature. The biggest assumption is that IrMn has a collinear AFM order in any phase, most notably by O'Grady *et al.* [16] and others [17,18]. Another common problem comes from the ordered $L1_2$ $IrMn_3$ phase, where it is assumed that the spin ordering is independent of the crystal ordering or even completely ignored [19]. In some cases, experimental samples exhibit a structure with an ordering parameter of less than 1 while assuming a 100% ordered structure [13,20]. The magnetic characteristics of IrMn are particularly important when considering the dynamics of devices [21,22], exchange bias [23,24], and electrical effects [17,25,26].

Here we present atomistic simulations of the equilibrium thermodynamic magnetic properties of Ir_xMn_{1-x} alloys as a function of their chemical composition and crystallographic ordering. Specifically, we study the composition dependence of the AFM ordering (Néel) temperature, ground-state spin structure, and magnetic anisotropies of the main ordered and disordered phases of IrMn.

II. METHOD

The starting point for modeling an AFM model at the atomistic level is a classical spin model, where each magnetic site is approximated as having a fixed length local magnetic moment μ_s. The direction of each spin i is described by a classical unit vector $\mathbf{S}_i$. The energetics of the IrMn system are described a spin Hamiltonian neglecting nonmagnetic contributions and

given by

$$\mathscr{H} = -\sum_{i<j} J_{ij}\mathbf{S}_i \cdot \mathbf{S}_j - \frac{k_N}{2}\sum_{i\neq j}^{z}(\mathbf{S}_i \cdot \mathbf{e}_{ij})^2, \qquad (2)$$

where $\mathbf{S}_i$ is a unit vector describing spin direction on Mn site i, k_N is the Néel anisotropy constant, and $\mathbf{e}_{ij}$ is a unit vector from site i to site j, z is the number of nearest neighbors (NNs) and J_{ij} are pairwise exchange interactions. The specific numerical values and assumptions for the range of exchange interactions and use of the Néel pair anisotropy model are described in detail in the following sections.

The equilibrium thermodynamic properties of the system of spins is simulated using the metropolis Monte Carlo method [27,28] with an adaptive step size [29] for optimal efficiency and rapid convergence to a thermodynamic equilibrium state. In this paper, the simulations were performed with the VAMPIRE software package [27,30].

The Néel temperature is central to our investigations. For computational efficiency, we use two approaches: direct calculation from the temperature dependence of the sublattice magnetization and from the temperature dependence of the susceptibility. The former is computationally efficient for the calculation of bulk properties but cannot be used to evaluate the order parameter of finite-size systems. In this case, the Néel temperature is calculated as the peak in the sublattice longitudinal susceptibility.

The sublattice magnetization n_α is the sum of the normalized magnetization of every atom in that sublattice:

$$n_\alpha = |\mathbf{n}_\alpha| = \left|\frac{1}{N_\alpha}\sum_{i}^{N_\alpha}\mathbf{S}_i\right|, \qquad (3)$$

where N_α is the number of atoms in a sublattice (α) and $\mathbf{S}_i$ is the spin direction of atom i. The Néel temperature was determined from the sublattice magnetization against temperature data by fitting the sublattice magnetization to

$$n = \langle n_\alpha \rangle = \left(1 - \frac{T}{T_N}\right)^\beta. \qquad (4)$$

To calculate the temperature dependence of the sublattice magnetization, we simulated a 6 nm × 6 nm × 6 nm system initialized at zero Kelvin. The temperature was slowly increased to 1200 K (above the predicted Néel temperature of the material) in 10 K steps. At each temperature step, the system was integrated for 100 000 Monte Carlo steps. The resulting mean sublattice magnetizations at each temperature step are plotted in Fig. 2 for each of the three sublattices. The mean sublattice magnetization is slightly above zero after the Néel temperature because of the finite size of the system.

The Néel temperature for each sublattice was calculated as 980 ± 15 K with an exponent $\beta = 0.32 \pm 0.03$, where the error is that in the fitting. The β exponent computed here is the same as seen for FMs [31] (where $\beta = 0.34 \pm 0.02$), suggesting that the shape of the (sublattice) magnetization in the vicinity of the ordering temperature has some characteristics of universality for 3D classical spin models, at least in the case of highly ordered alloys. The three sublattices all have the same Néel temperature and so the total sublattice
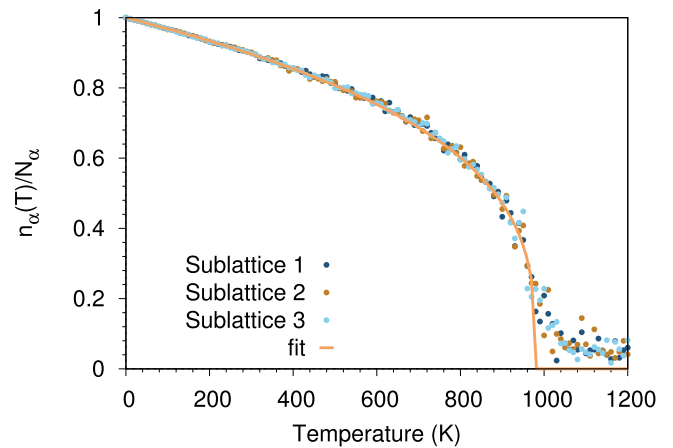

FIG. 2. The variation of sublattice magnetizations with temperature in ordered $L1_2$-IrMn$_3$. The curve was fit to the simulated data using Eq. (4). The Néel temperature for each sublattice was (980 ± 15) K with the error determined from the curve fit. The order of an antiferromagnet can therefore be characterized by looking at the individual sublattice magnetization.

magnetization of the material is equal to the average sublattice magnetization. In some cases where different degrees of order are present, one or more of the sublattices may have a different Néel temperature, and so a mean value for the sublattice magnetization or Néel temperature is not meaningful.

For finite system sizes, a more rigorous way of calculating the Néel temperature is from the magnetic susceptibility. We calculate the isotropic longitudinal susceptibility for each sublattice from the standard fluctuation formula [32] as

$$\chi_\alpha = \frac{\sum_{i=0}^{N_\alpha}\mu_i}{k_B T}(\langle |n_\alpha|^2\rangle - \langle |n_\alpha|\rangle^2), \qquad (5)$$

where i are indices of atoms within the same sublattice α. We note that the usual directionality in the susceptibility is removed here, and we only consider fluctuations in the *length* of the sublattice magnetization, hence the terminology of isotropic susceptibility. Furthermore, the susceptibility scales with the number of moments considered, while the strength of the sublattice magnetization fluctuations scales with the inverse number of spins, leading to a largely size-independent susceptibility, though small differences appear due to finite-size effects [33]. Figure 3 shows the simulated temperature-dependent average sublattice susceptibility $\overline{\chi} = (\chi_1 + \chi_2 + \chi_3)/3$ for a $(10 \text{ nm})^3$ cube of $L1_2$-IrMn$_3$ showing the usual decrease in sublattice spin order with increasing temperature due to spin fluctuations. The sublattice susceptibility diverges at the Néel temperature with a well-defined peak from which we extract T_N. The isotropic susceptibility has the same form for AFMs as for FMs, and quite different from the form for isotropic 1D and 2D AFMs [32] due to the presence of large magnetocrystalline anisotropy in the IrMn system [34].

In the following, for reasons of computational efficiency, we use the fitting method to calculate the Néel temperature of bulk systems and the susceptibility for finite-size systems.
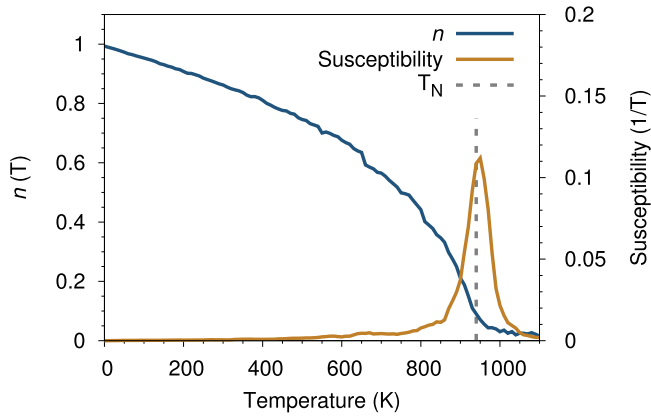
FIG. 3. The average sublattice magnetization $\bar{n}$ and isotropic longitudinal susceptibility $\bar{\chi}$ as a function of temperature for the L1$_2$ phase of IrMn$_3$. The Néel temperature T_N is extracted from the peak in the susceptibility and is close to the bulk value [13] of 950 K. The susceptibility follows the usual shape seen for ferromagnets, with a single well-defined peak near the Néel temperature.

III. ATOMISTIC SPIN MODEL OF IRIDIUM MANGANESE

The complicated behavior of AFM materials in general, but specifically complex AFMs such as IrMn, limits the applicability of simple modeling approaches such as two-sublattice AFM or micromagnetic models. Previous *ab initio* simulations of IrMn alloys have determined ground-state spin structures and effective exchange constants and magnetic anisotropies for the pure ordered L1$_2$ and L1$_0$ phases [14,15,35], and effective exchange constants for the disordered γ phase [14]. While such calculations are essential for understanding the underlying electronic properties of IrMn$_3$, they are limited to idealistic cases, very small numbers of atoms, and static properties only. In disordered IrMn alloys, each atom has a different local environment, with different numbers of Mn and Ir neighbors in different crystallographic positions. First-principles *ab initio* simulations of alloys typically use the coherent potential approximation [14], which uses an ordered lattice of averaged potentials to replace the spatially varying potential. While this enables the determination of fundamental properties such as ground-state spin structures, exchange constants, and anisotropies, it neglects the fundamental disordered nature of the crystal, where the local spin structure will have distortions based on the exact local crystallographic structure. This is particularly important when introducing defects into the system [33] or at interfaces when considering exchange bias effects [23] where the specific details of the atomic structure dominate the physical behavior. In nanoscale devices, the details of the atomic structure, crystallographic ordering, grain boundaries, interfaces, defects, elevated temperatures, and dynamics each play a critical role in determining the overall properties and dynamic response. Here we present a minimal but detailed atomistic spin model that encapsulates the essential physics of Ir$_x$Mn$_{1-x}$ alloys allowing simulations of time and temperature-dependent properties of nanoscale devices.
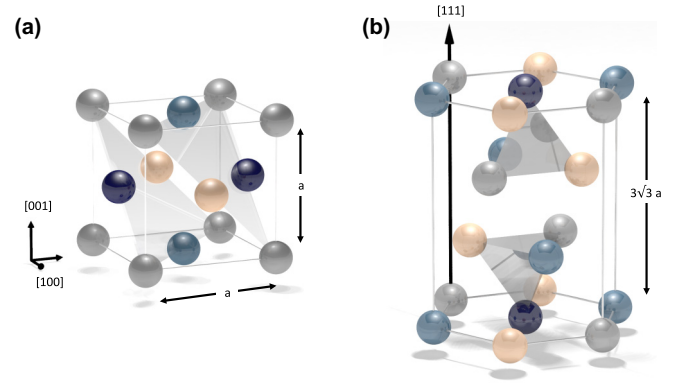

FIG. 4. Visualizations of the unit cell structure of iridium manganese. (a) The fcc unit cell structure of iridium manganese in the [001] plane orientation. a is the unit cell length. The (111) planes are shaded in grey. (b) The (111) oriented fcc crystal structure. The colors represent the four magnetic sublattices present in iridium manganese.

A. Crystallography

The first step is to create an accurate lattice structure for iridium manganese alloys. Iridium manganese has previously been observed in many crystallographic phases. Most notably, the L1$_0$, L1$_2$, and γ phases. These phases all appear quite distinct as the Ir and Mn atoms are in different positions within the unit cell, leading to different crystallographic and magnetic structures. However, the majority of these structures have an underlying face-centered cubic (fcc) lattice, or in the case of L1$_2$ with a small distortion along the (001) crystal direction to give a face-centered tetragonal (fct) structure [14,15]. The fcc lattice occurs because the iridium atoms are larger than the Mn atoms, increasing the lattice spacing. For all compositions with Mn concentrations less than 95%, the structure can be said to be based on a base fcc structure. For concentrations of Mn greater than 95%, the magnetic structure changes to α-Mn that has a complex allotropic structure with 58 atoms in the unit cell [36]. As the compositions used in spintronic devices have approximately 17–25% Ir, we can generally assume that the IrMn will have a base fcc structure.

The fcc unit cell of iridium manganese is comprised of four atoms—with a (001) out-of-plane orientation this forms the structure shown in Fig. 4(a). The unit cell length (a) for IrMn$_3$ is approximately 0.375 nm but this depends on the composition and order of the crystal [13]. Iridium manganese can be grown in many different crystallographic orientations depending on the seed layer used in the sputtering process. Although these all give an observable exchange bias, the largest exchange bias occurs in samples grown with a (111) structure. To maximize the exchange bias and reproduce the thin films used in spintronic devices, the crystal structure needs to be reoriented to lie so the (111) direction points out of plane, shown in Fig. 4(b).

Iridium manganese has a complex magnetic structure containing up to four magnetic sublattices. The moments of the atoms in different sublattices prefer energetically to

align antiparallel due to the AFM nature of the exchange interactions. Instead, the ground states form complex frustrated spin structures when more than two sublattices are present due to symmetry. An analogous effect occurs in the structure of molecules, where atoms are bonded together but repel each other due to electronic charges. Thus, diatomic molecules form $\theta = 180°$ bonds, homonuclear triatomic molecules such as H_3 form planar molecules $\theta = 120°$, and tetranuclear molecules such as As_4 or CH_4 from a tetrahedral structure $\theta = 109.5°$. The structure of AFMs follows the same principle, with the structure defined by the strength of the interactions and symmetry. In Fig. 4, the magnetic sublattices are highlighted by the different colors and the tetrahedron contains one atom from each AFM sublattice, containing all the magnetic information of the crystal.

The ordering of iridium manganese depends on the placement of the Ir atoms within the Mn lattice. In ordered iridium manganese, the Ir atoms are all in the same sublattice and in disordered iridium manganese the Ir atoms are equally spread throughout the four sublattices. In disordered iridium manganese, the random removal of atoms means the crystal has no repeating structure and cannot be simplified to the 24-atom unit cell. In the $IrMn_3$ composition, 75% of the atoms are Mn and 25% of the atoms are Ir. In ordered $IrMn_3$ this means one sublattice is completely Ir and three sublattices are completely Mn, while in disordered γ-$IrMn_3$ 25% of the atoms in each sublattice are Ir and 75% of the atoms in each sublattice are Mn.

B. Magnetic moments

As the starting point for our atomistic model description, we assume that each atom possesses a magnetic moment located on the lattice site. For strong magnetic moments such as Fe, Co, and Mn, this is generally a good approximation, where the local spin density is strongly localized around the nucleus. *Ab initio* calculations [15,37] found local Mn moments of $\mu_s = 2.6 \pm 0.02$ μ_B for the ordered phases and $\mu_s \sim 2.48 \pm 0.03$ μ_B for the disordered γ-$IrMn_3$ phase, 5% lower than the ordered phase. As the moments do not strongly depend on the ordering or composition, we have assumed a fixed moment of $\mu_s = 2.6$ μ_B commensurate with the ordered phases.

C. Exchange interactions

Ab initio calculations by Szunyogh *et al.* calculated the exchange interactions for ordered IrMn and $IrMn_3$ phases and found an oscillatory dependence on the interatomic spacing (R_{ij}). The variation is shown in Fig. 5 with data taken from Ref. [15] and shows the exchange coupling switches from positive (FM) to negative (AFM) with each incremental neighbor shell. The NN interactions are strongly AFM and the next nearest neighbor (NNN) interactions are weaker and FM in nature. Importantly, the NN interactions occur between atoms in different magnetic sublattices whereas the NNN interactions occur between atoms in the same sublattice. The FM NNN interactions are therefore important because they tend to stabilize the magnetic structure and long-range AFM ordering of IrMn. The exchange interactions are only
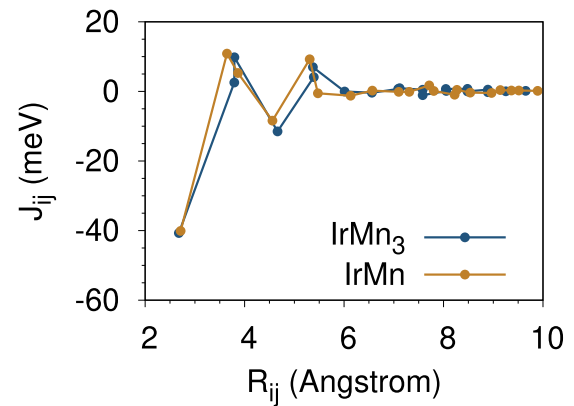

FIG. 5. *Ab initio* data from Ref. [15] showing the variation of the exchange constants in IrMn and $IrMn_3$ vary with interatomic spacing (R_{ij}). The data was calculated using the relativistic torque method. The exchange constants periodically vary between positive (FM) and negative (AFM) with interatomic spacing. The first set of points represents the nearest neighbor (NN) interaction and the second set of points represents the next nearest neighbor (NNN) interaction; this pattern continues.

significant for the first four NN shells, listed for the $L1_2$ phase in Table I. The interactions can all be summarized by AFM (negative) interactions between atoms in different sublattices and FM (positive) interactions between atoms in the same sublattice. If all these exchange interactions are included, there will be over 50 terms per atom, making simulations computationally expensive and therefore limiting the length and timescales accessible. This is particularly important when considering large scale or long simulations such as those used for exchange bias [23]. To decrease the computational power required, we therefore approximate the exchange interactions including only NN and NNN interactions.

Deleting the longer ranged exchange interactions naturally decreases the Néel temperature, and so the reduction in complexity was achieved by changing the J_{ij}^{NNN} interaction strength to account for the third and fourth NN interactions while keeping J_{ij}^{NN} constant at the calculated *ab initio* value of -6.4×10^{-21} J. This reduces the number of terms in the Hamiltonian to only 18 and 12 NN interactions and 6 NNN interactions. To calculate the new J_{ij}^{NNN}, magnetization versus temperature, curves were simulated for varying values of J_{ij}^{NNN} for the $L1_2$ ordered phase until T_N matched the value of $T_N = 950$ K calculated using all the nonzero interactions, previously shown in Fig. 3. For each value of J_{ij}^{NNN}, T_N was calculated from the sublattice magnetization. The simulated

TABLE I. The nonzero exchange interactions in IrMn calculated by Szunyogh *et al.* [15] and the number of neighbors at each distance.

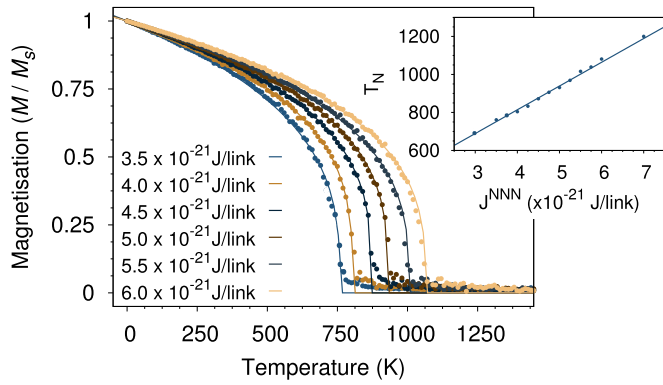| Neighbor	Energy (J/link)	Number of neighbors
First	-6.4×10^{-21}	12
Second	$+1.12 \times 10^{-21}$	6
Third	-1.6×10^{-21}	24
Fourth	$+0.9 \times 10^{-21}$	12

FIG. 6. The simulated Néel temperature for different values of J_{ij}^{NNN} for $L1_2$-IrMn$_3$. To find the value of J_{ij}^{NNN} for IrMn, the Néel temperature was calculated for different values of J_{ij}^{NNN} for $L1_2$-IrMn$_3$. This was compared to the known value (≈ 1000 K) which has been measured via neutron scattering [13]. The value was varied around that found by Szunyogh *et al.* [15]. The T_N was calculated by cooling a sample from $T > T_N$ and calculating the magnetization of the sample at each point when the magnetization is zero, this is T_N. The simulated curves were fit using Eq. (4) as shown. (b) The variation of T_N with J_{ij}^{NNN}, the points are the calculated T_N values, these were fit using a linear function.

sample was 8 nm $\times$ 8 nm $\times$ 8 nm with periodic boundary conditions with the same simulation parameters. The simulated data and the fit curves are shown in Fig. 6. The simulated T_N matches the known value when $J_{ij}^{\text{NNN}} = +5.61 \times 10^{-21}$ J, which is the value we adopt for the remainder of this paper.

An important characteristic of the long-range exchange interactions is that the exchange interactions are approximately the same magnitude for both ordered $L1_0$-IrMn and ordered $L1_2$-IrMn$_3$ phases. These alloys both have very different compositions and crystal symmetry but this has not greatly affected the exchange interactions. As a first approximation, we therefore assume that the pairwise exchange interactions are identical for all compositions and orders studied in this paper.

D. Magnetic anisotropy

In disordered IrMn alloys, determination of the anisotropy term in the spin Hamiltonian presents a significant challenge, as each atom has a different local crystalline environment, leading to a unique anisotropy value at each site. It has been suggested that a loss of crystal symmetry could result in a reduction in the local anisotropy [38]. Ideally, the loss of anisotropy would be modeled using a completely *ab initio* approach, but this is only feasible for up to a few 100 atoms and, consequently, is an unrealistic approach to model a realistic size AFM system of millions of atoms. Instead, the Néel pair anisotropy model is used, a model first proposed by Néel in 1954 [38] to model the surface of a crystal. The model assumes that the lack of bonds at surfaces causes an anisotropy. We have extended the Néel pair anisotropy model to model the nonmagnetic Ir atoms as nonmagnetic impurities. The magnetocrystalline anisotropy arises from a complex interaction between the spin-orbit coupling and the local atomic environment represented by

the crystal field. Akhiezer *et al.* [39] proposed a formulation of the spin-orbit coupling suitable for spin models. This has a form similar to a dipolar coupling, specifically $\mathscr{H}_c = -\sum_{i,j} f(r_{ij})[(\mathbf{S}_i \cdot \hat{\mathbf{r}}_{ij})(\mathbf{S}_j \cdot \hat{\mathbf{r}}_{ij}) - \frac{1}{3}\mathbf{S}_i \cdot \mathbf{S}_j]$. $f(r_{ij})$ determines the degree of localization, and the second, exchangelike, term is included to preserve the Curie temperature of the system and to ensure no net anisotropy when the atoms form a symmetric cubic lattice. This form of coupling is currently finding application in models of spin lattice dynamics [40]. Anisotropy arises when there is some symmetry breaking, for example, in the case of an applied stress. Here, the symmetry breaking arises from the presence of the nonmagnetic Ir atoms, leading to a single-site anisotropy which we express in the form of a Néel anisotropy, which removes the necessity for an exchange-like term present in the pseudodipolar anisotropy. We also assume that the anisotropy is highly localized, requiring only a summation over NNs.

The physical justification for this approach comes from the competition of the quenching from the crystal field and the unquenching from spin-orbit coupling. Quenched waves naturally have a standing wave character and therefore adapt more easily to the crystal field and induce a lower magnetocrystalline anisotropy. The size of the crystal field is caused by the symmetry in the crystal and the Ir atoms in the system naturally break this symmetry, meaning that the Mn orbitals will be more quenched in some directions (pointing toward Mn atoms) than in others (pointing toward Ir atoms) [41]. The Ir atoms have a very large spin-orbit coupling, which reduces the quenching of the electron density for nearby Mn atoms. Therefore, it is lower energy for a spin to point in some directions (near the Mn atoms) than in others (near other Ir atoms).

In our model, the iridium atoms are considered as nonmagnetic bulk impurities, generating an effective magnetic anisotropy that is equivalent to the missing bonds at the surface in the Néel pair anisotropy model [42]. The minimum energy is found when the moments point away from the iridium atoms. The pair anisotropy can be described by the following contribution to the spin Hamiltonian:

$$\mathscr{H}_N^i = -\frac{k_N}{2} \sum_{ij}^{z_i} (\mathbf{S}_i \cdot \mathbf{e}_{ij})^2, \qquad (6)$$

where $\mathbf{e}_{ij}$ is a unit vector connecting spin i with its z nearest Ir neighbors j and k_N is the Néel pair anisotropy constant between Ir and Mn atoms. The form of Eq. (6) naturally leads to a configurational magnetic anisotropy that depends on the local crystal symmetry around each Mn site. The anisotropy surfaces for three different environments are shown in Fig. 7. Each configuration shows the Mn atom sitting in a completely different anisotropy environment based on the local crystal symmetry. If each atom in the crystal has a unique anisotropy, the local anisotropy cannot be simply expressed as an average anisotropy at each site. The sitewise differences in the local anisotropy are particularly important in determining spin frustration in exchange-biased systems [23]. In the disordered and of-stochiometric phases of IrMn, the effective anisotropy will always be a superposition of the local anisotropies of individual Mn sites, with the addition of local spin deviations from the average magnetic structure caused by local Mn
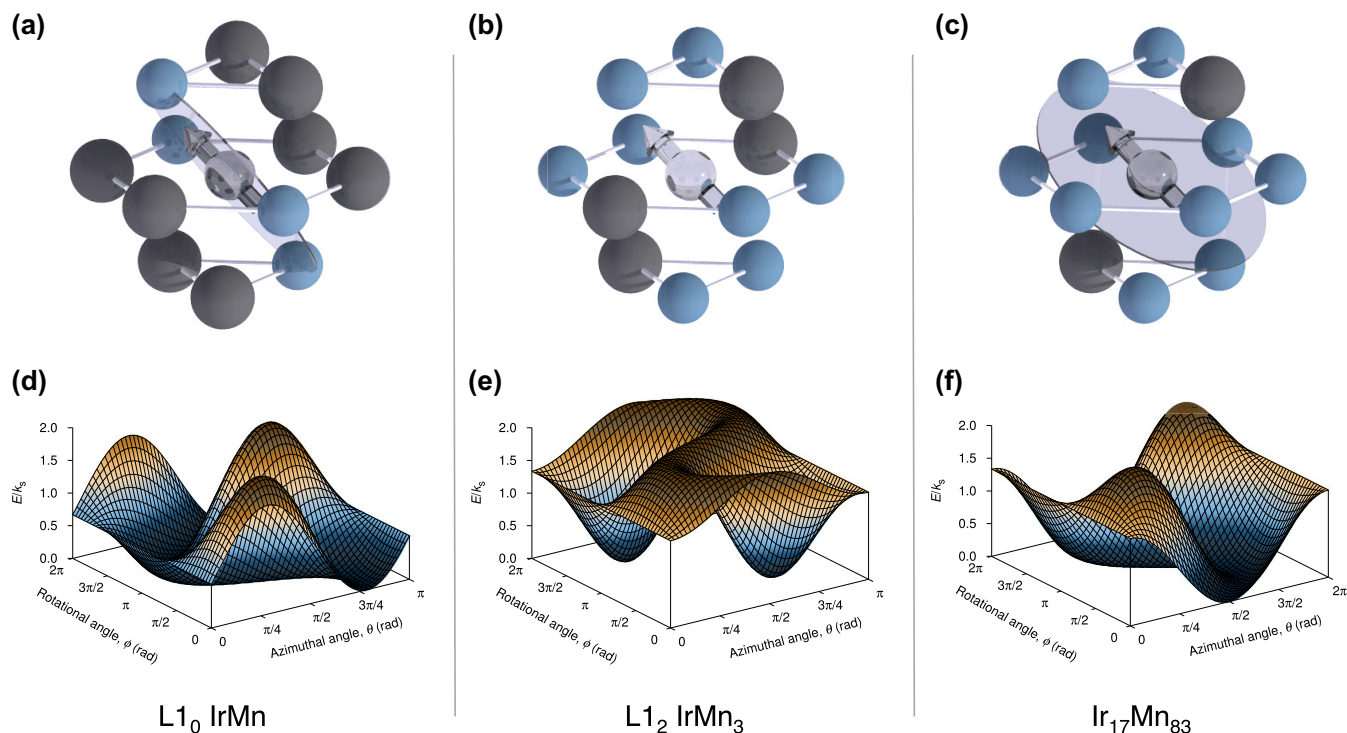
FIG. 7. Local atomic configurations and anisotropic energy surfaces for different IrMn compositions calculated with the Néel pair anisotropy model. The form and anisotropy energy in IrMn is strongly dependent on the local atomic ordering. In disordered crystal structures, this leads to a complex energy surface with highly localized variations of the magnetic anisotropy. (a) Spin configuration for ordered $L1_0$-IrMn, which has (d) an easy plane anisotropy. (b) Spin configuration for ordered $L1_2$ which (e) has a complex energy surface. (c) Spin configuration for an off-stochiometric composition (f) which has a complex energy surface.

symmetries. Ideally, one would calculate the anisotropy of each individual lattice site using *ab initio* methods but, unfortunately, using current methods, the computational resources necessary would be too large, needing to consider thousands of spins.

The value of the anisotropy constant in IrMn is a widely disputed problem with experimental and theoretical calculations varying by over two orders of magnitude. Szunyogh *et al.* performed self-consistent calculations using the fully relativistic screened Korringa-Kohn-Rostoker method [15]. They found an extremely large second-order magnetic anisotropy for IrMn$_3$, leading to energy barriers of the order of 300 $\times 10^5$ J/m^3 [43]. Vallejo-Fernandez *et al.* inferred the anisotropy constant of the IrMn experimentally by measuring the mean blocking temperature (T_B) of an IrMn/CoFe bilayer. They inferred a value of the anisotropy constant of $(5.5 \pm 0.5) \times 10^5$ J/m^3 [43] almost two orders of magnitude lower than the theoretical calculation. The symmetry of the anisotropy in IrMn$_3$ is also debated. Szunyogh *et al.* [15] calculated the anisotropy to be cubic in symmetry and Vallejo-Fernandez *et al.* [43] inferred the temperature dependence of the anisotropy energy to have a uniaxial symmetry from the Callen-Callen laws [44]. Later we demonstrate that this difference comes from the problem in defining the bulk anisotropy of an AFM, and so we adopt the value of $k_N = -4.2 \times 10^{-22}$ J/link from the *ab initio* calculations.

To verify the correctness of our model, we made a direct comparison of the calculated rotational anisotropy determined from *ab initio* calculations of Szunyogh *et al.* [15]. Our model

was tested by rotating the moment of a Mn atom around the (111) plane of ordered $L1_2$-IrMn$_3$. The change in energy calculated using Eq. (6) exactly matches the *ab initio* result both in symmetry and magnitude, confirming the equivalence of the Néel pair anisotropy model and the full *ab initio* approach in the case of ordered $L1_2$-IrMn$_3$ as shown in Fig. 8. From
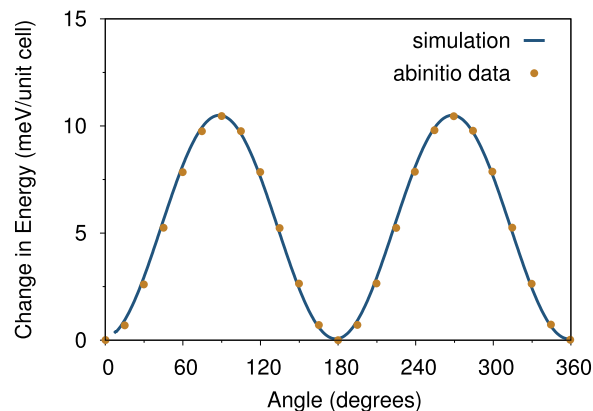

FIG. 8. Simulation to calculate the change in energy when a spin is rotated around the 111 plane and compared to the *ab initio* result by Szunyogh *et al.* [15]. The points are the *ab initio* data and the line is the data simulated using Eq. (6). The simulated result and *ab initio* data both have a $\sin^2(\alpha)$ energy dependence. The $\sin^2(\alpha)$ energy dependence is due to the spin having a high anisotropy energy when it rotates toward the large orbitals of the Ir atoms.

TABLE II. Final parameters used in the atomistic spin model of Ir_xMn_{1-x} alloys.

Quantity	Symbol	Value	Unit
Nearest-neighbor exchange	J_{ij}^{NN}	-6.4×10^{-21}	J/link
Next-nearest-neighbor exchange	J_{ij}^{NNN}	$+5.1 \times 10^{-21}$	J/link
Néel pair anisotropy	k_N	-4.2×10^{-22}	J/link
Magnetic moment	μ_s	2.60	μ_B

here we assume that the Néel pair anisotropy constant is primarily a function of spin-orbit coupling and lattice symmetry and we neglect second-order effects arising due to lattice distortions. The final model parameters for moments, exchange interactions, and anisotropy used in this paper are summarized in Table II.

IV. GROUND-STATE SPIN STRUCTURES

To verify our model, we have studied the AFM properties of the ordered and disordered IrMn₃ alloys for a single crystal bulklike 8 nm × 8 nm × 8 nm sample with periodic boundary conditions applied. The temperature-dependent magnetization was investigated from 0 K to $T > T_N$ to verify agreement with the experimental and *ab initio* data for the Néel temperatures and 0 K magnetic structure. The system is first equilibrated for 10 000 Monte Carlo steps at each temperature (taking the final configuration from the previous temperature as a starting point) and then 100 000 averaging Monte Carlo steps are performed to evaluate statistical averages. Figure 9(a) shows the simulated 0 K ground-state magnetic structures where the ordered alloy forms a triangular (T1) spin structure with an angle of 120° between adjacent spins and the disordered alloy forms a tetrahedral (3Q) spin structure with 109.5° between spins in agreement with previous neutron scattering experiments [12,13] and theoretical calculations [15]. The simulations predict different Néel ordering temperatures for the ordered and disordered phases of 1005 K and 688 K, respectively, shown in Fig. 9(b). This is in close agreement with experimental values of 730 K [11] and 960 K [12] for γ and L1₂ phases, respectively. The stark difference in the ordering temperature for the different phases of IrMn₃ is surprising given the same composition and the same number of exchange bonds per Mn atom. The explanation lies in the different degrees of frustration for the different compositions.

As an AFM, IrMn prefers a perfect antiparallel 180° alignment of Mn moments. Due to the lattice symmetry in the L1₂ and γ phases, perfect 180° alignment of spins is not possible, leading to a frustrated spin state with reduced symmetry. This intrinsic frustration leads to a natural reduction in the effective exchange energy due to the increased angle between spins in the ground state and commensurate reduction in the Néel temperature. Quantitatively, this can be expressed in terms an effective exchange coupling as a function of the angle between sublattices θ from Eq. (1). For an AFM, the minimum energy occurs for $\theta = 180°$, giving an energy difference between the AFM and FM states as $2J_{ij}$. However, in the paramagnetic state (above the Néel temperature), the $\theta = 0°$ state is still extremely high energy due to local spin correlations and so a
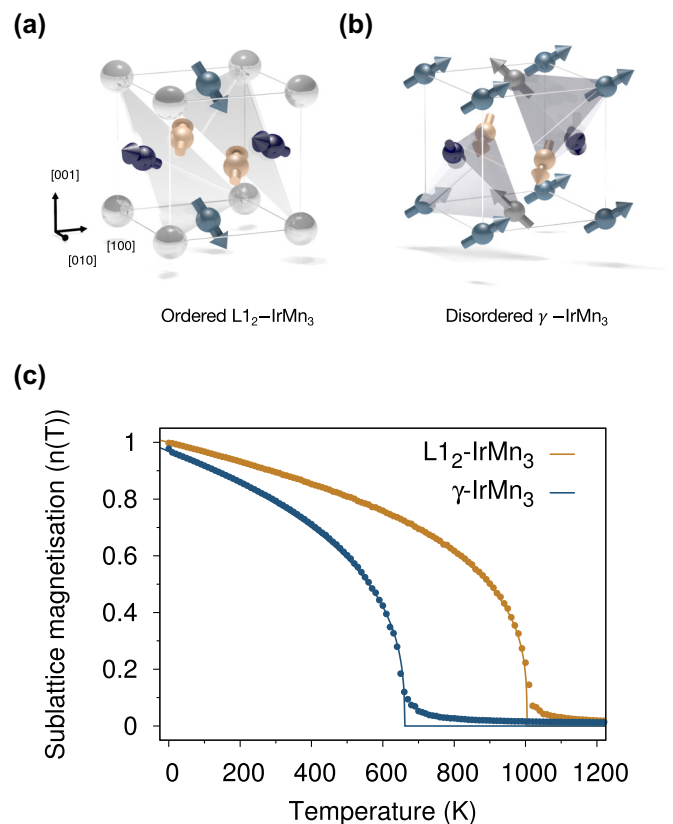

Ordered L1₂–IrMn₃   Disordered γ–IrMn₃

FIG. 9. Simulated ground-state magnetic structures and temperature-dependent ordering for the ordered and disordered phases of IrMn₃ showing triangular and tetrahedral order, respectively. (a) The ground-state structures are obtained by simulated zero-field cooling for the ordered L1₂ and disordered γ-IrMn₃ phases showing triangular (T1) and tetrahedral (3Q) spin order, respectively. (b) Simulated temperature-dependent sublattice magnetizations for the different phases of IrMn₃. Lines show fits to the sublattice magnetization n(T) given by $n(T) = (1 - \frac{T}{T_N})^\beta$, where T is the temperature, T_N is the Néel (ordering) temperature, and $\beta \approx \frac{1}{3}$ is the magnetization critical exponent. The ordered phase has a Néel temperature of 1005 K, while the disordered phase has a significantly reduced Néel temperature of 688 K arising from increased magnetic frustration in the disordered phase. The spin ordering in the disordered phase is only partial at low temperatures, indicating the presence of intrinsic spin disorder.

more realistic value of the mean angle for the paramagnetic state is $\langle\theta\rangle \sim 0°$. On this basis, the Néel temperature can be correlated with the exchange energy difference between the ordered $\theta = 180°, E = -J_{ij}$, and $\theta = 0°, E = 0$ paramagnetic state. For the L1₂ phase with $\theta = 120°$, this gives an exchange energy difference of $|J_{ij}\cos(120°)| = \frac{1}{2}J_{ij}$. For the γ phase with $\theta = 109.5°$, this gives an exchange energy difference of $|J_{ij}\cos(109.5°)| = \frac{1}{3}J_{ij}$. Thus, one would expect a fractional change in the Néel temperature of $\frac{1}{3}/\frac{1}{2} = \frac{2}{3}$ which agrees almost perfectly with the observed decrease from 1005 K for the L1₂ phase to 688 K for the γ phase.

Now that we have validated our model of IrMn against previous experimental and theoretical results, we proceed to investigate different orders and compositions. Due to the theoretical complexity of modeling a disordered structure,

TABLE III. The percentage of each sublattice that is made up of Mn atoms depending on the order and composition of the structure.

Order parameter	Sublattice 1	Sublattice 2	Sublattice 3	Sublattice 4	D/D_d
1.0	100%	100%	100%	0%	0.0
0.8	95%	95%	95%	15%	0.2
0.6	90%	90%	90%	30%	0.4
0.4	85%	85%	85%	45%	0.6
0.2	70%	70%	70%	60%	0.8
0.0	75%	75%	75%	75%	1.0

previously only the properties of the ordered states of IrMn and disordered IrMn$_3$ have been extensively investigated. However, using our estimates of the exchange and the Néel pair anisotropy model, we can study any order or composition. In the next section, a full study of the properties with composition and order will be made. Initially, IrMn$_3$ will be investigated with a full phase study between the ordered and disordered states. Subsequently, a full phase study will be undertaken for all compositions of the completely ordered and completely disordered alloys.

V. PARTIALLY ORDERED IrMn$_3$ ALLOYS

In this section, the Néel temperature of the partially ordered phases of IrMn$_3$ are investigated. Fully ordered, the probability of finding Mn in sublattices 1, 2, and 3 is unity. In the disordered state, Mn is replaced uniformly by Ir, leading to a probability of 0.75 to find the sublattice-4 sites occupied by Mn. Thus, we define an order parameter O given by

$$O = 1 - \frac{D}{D_d}, \qquad (7)$$

which is a function of D/D_d, where (D) is the percentage of Mn in sublattice 4, and (D_d) is the percentage of Mn in sublattice 4 in the fully disordered system (75%). The Néel temperature was simulated for the six compositions outlined in Table III. The system was 8 nm × 8 nm × 8 nm and the Néel temperature was calculated by fitting to the magnetization.

The temperature-dependent magnetization was investigated from 0 K to $T > T_N$. The system is first equilibrated for 10 000 Monte Carlo steps at each temperature (taking the final configuration from the previous temperature point) and then 100 000 averaging Monte Carlo steps are performed where statistical averages are calculated. Between the ordered and disordered phases of IrMn$_3$, the Néel temperature decreases linearly from 1005 K for $L1_2$-ordered IrMn$_3$ to 690 K for the disordered phase.

We have calculated the Néel temperature as a function of the order parameter, the results being shown in Fig. 10(a). It can be seen that T_N increases linearly with order parameter. To understand the origin of the linear variation, we look at the underlying spin structure. The ordered $L1_2$ phase has a triangular structure with the sublattice magnetizations oriented at 120° whereas the disordered γ phases forms a tetragonal spin structure with 109.5° between the sublattices. The angle relates directly to the level of frustration in the system: the increased angle between spins reducing the strength of
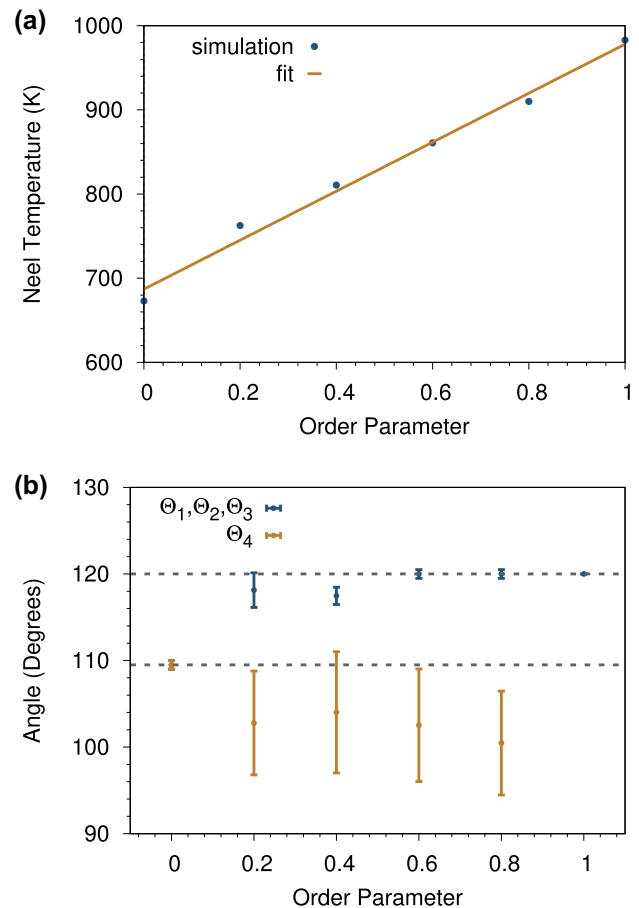

FIG. 10. (a) The calculated Néel temperatures for different order parameters in IrMn$_3$. (b) The angle between the sublattices for different order parameters. The blue dots represent the average angle between sublattices 1, 2, and 3. The yellow dots represent the average angle from sublattice 4 to the other three sublattices. The error bars are the standard deviation of the angles. 109.5° and 120° are shown as dotted lines on the diagram as these are the angles of the fully ordered and fully disordered phases.

the effective exchange coupling. The average angles between each sublattice pair are plotted in Fig. 10(b). For the phases between complete order and disorder, there is a large difference between the angles between sublattices 1, 2, and 3 and the angles of these three sublattices with sublattice 4. The difference occurs because sublattices 1, 2, and 3 all contain the same percentage of Mn atoms whereas sublattice 4 contains a different percentage. To clarify this, two angles are calculated: the average angle between sublattices 1, 2, and 3 ($\theta_{1,2,3}$), and the average angle from sublattice 4 to the other three sublattices (θ_4). $\theta_{1,2,3}$ is almost exactly 120° for all phases apart from the completely disordered phase. This suggests that the ground state has tended toward the triangular ground state of the ordered phase. θ_4 varies a larger amount and is not between 109.5 and 120, suggesting a large amount of frustration in the structure. In all but the fully disordered phase, the temperature dependence of the sublattice magnetization for sublattice 4 is significantly stronger than the others, with a much lower Néel temperature. Therefore, the linear reduction in the Néel temperature for the main three sublattices is mainly due to the loss

TABLE IV. The percentage of manganese was increased by maintaining as many filled sublattices as possible; these values will be used to see how increasing the percentage of manganese changes the Néel temperature.

Composition	Sublattice 1	Sublattice 2	Sublattice 3	Sublattice 4
$Ir_{75}Mn_{25}$	100	0	0	0
$Ir_{70}Mn_{30}$	100	20	0	0
$Ir_{65}Mn_{35}$	100	40	0	0
...	:	:	:	:
$Ir_{50}Mn_{50}$	100	100	0	0
$Ir_{45}Mn_{55}$	100	100	20	0
$Ir_{40}Mn_{60}$	100	100	40	0
...	:	:	:	:
$Ir_{25}Mn_{75}$	100	100	100	0
$Ir_{20}Mn_{80}$	100	100	100	20
$Ir_{15}Mn_{85}$	100	100	100	40
...	:	:	:	:
Mn	100	100	100	100

of exchange bonds as sublattice 4 becomes more magnetic. This has a negligible impact on the ground-state spin structure of the partially ordered IrMn$_3$ alloy and suggests that the assumption of Kohn *et al.* that the ground state is largely the same for partial ordering [13] is a good one. Now that we have looked into partially ordered states, the completely ordered and completely disordered states with different compositions will be investigated.

A. Néel temperatures of ordered Ir_xMn_{1-x} alloys

In the following section, the Néel temperature and low temperature ground-state magnetic structure of Ir_xMn_{1-x} alloys will be calculated for compositions in the range $Ir_{75}Mn_{25}$ to Mn_{100}. The compositions investigated are outlined in Table IV, showing the percentage of Mn in each sublattice. As the percentage of Mn is increased, the sublattices fill up sequentially so each sublattice is filled with Mn atoms before the next sublattice contains any Mn atoms to preserve the ordered nature of the alloys. In these alloys, one sublattice typically contains a mixture of Ir/Mn atoms. Table IV shows that there are three fully ordered IrMn compositions: $Ir_{75}Mn_{25}$, $Ir_{50}Mn_{50}$, and $Ir_{25}Mn_{75}$. In these states, every sublattice is either Ir or Mn and there is no partial Ir/Mn sublattice. The properties of $Ir_{25}Mn_{75}$ (IrMn$_3$) have already been studied in depth in the previous section, however, so far $Ir_{75}Mn_{25}$ and $Ir_{50}Mn_{50}$ (Ir$_3$Mn and IrMn, respectively) have not been considered.

Figure 11(a) shows sublattice magnetization versus temperature curves for IrMn and Ir$_3$Mn. The ground-state structures of Ir$_3$Mn and IrMn are shown in Figs. 11(b) and 11(c), respectively. $Ir_{50}Mn_{50}$ has a Néel temperature of 1200 K and Ir$_3$Mn has a Curie temperature of 590 K. The Néel temperature of $Ir_{50}Mn_{50}$ is very high, even higher than IrMn$_3$, due to the absence of frustration in the spin structure, despite the loss of $\frac{1}{3}$ of the exchange bonds. $Ir_{50}Mn_{50}$ has the ground-state structure of a collinear AFM with no frustration as the sublattice magnetizations of the two Mn sublattices point 180° apart. The ground-state structure therefore explains the very high Néel temperature. The result
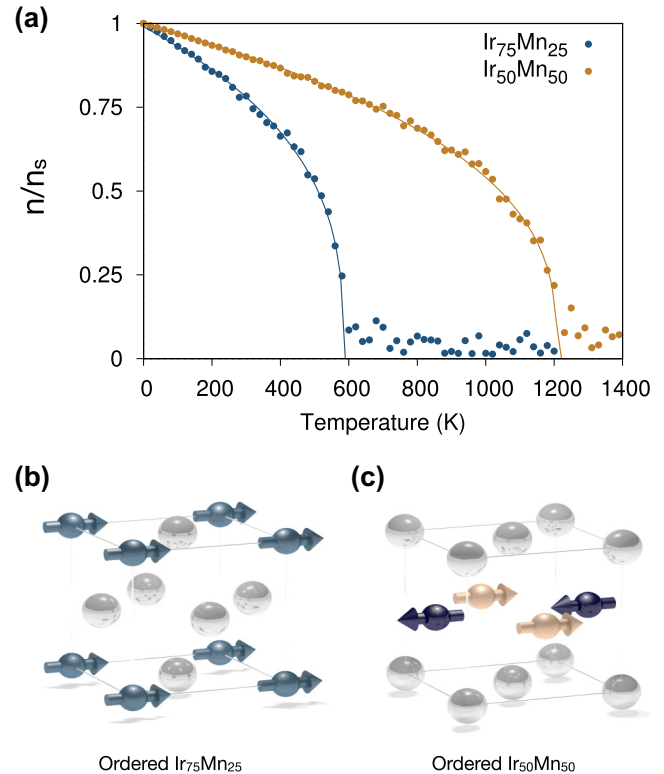

FIG. 11. Magnetization versus temperature curves and visualizations of the simulated ground-state spin structures for ordered IrMn and Ir$_3$Mn obtained from zero-field cooling. (a) Magnetization versus temperature curves show a Néel temperature of 584 K and 1209 K for IrMn and Ir$_3$Mn, respectively. Ground-state magnetic structures of (b) ordered Ir$_{75}$Mn and (c) ordered $Ir_{50}Mn_{50}$. The spins show an average spin of each magnetic sublattice direction over the whole sample. IrMn has a classic AFM structure with the sublattices pointing 180° apart whereas Ir$_3$Mn the magnetic structure is FM.

matches the in-plane anisotropy observed experimentally [45] and the ground-state spin structure matches that calculated via *ab initio* methods [15].

The ground state of Ir$_3$Mn is FM, which is perhaps surprising. The FM ground state occurs because in Ir$_3$Mn only one sublattice contains Mn atoms and the exchange coupling between atoms in the same sublattice is FM. The unfrustrated FM ground state explains the high Curie temperature even though the system is very diluted. Our prediction of a FM phase correlates well with the Pt$_3$Mn system which has a reasonably high Curie temperature of ~453 K [46]. Importantly, the Curie temperature of the ordered Ir$_3$Mn phase provides an experimental way to evaluate the strength of the NNN coupling in the Ir_xMn_{1-x} system.

Now that the properties of the completely ordered alloys have been investigated, we want to know what happens to the Néel temperature and ground-state spin structure between these compositions. An example sublattice magnetization versus temperature curve is shown in Fig. 12(a), where the curves have been plotted separately for all three sublattices. We notice that the Néel temperature of the diluted sublattice is much lower than the other three sublattices although it does still
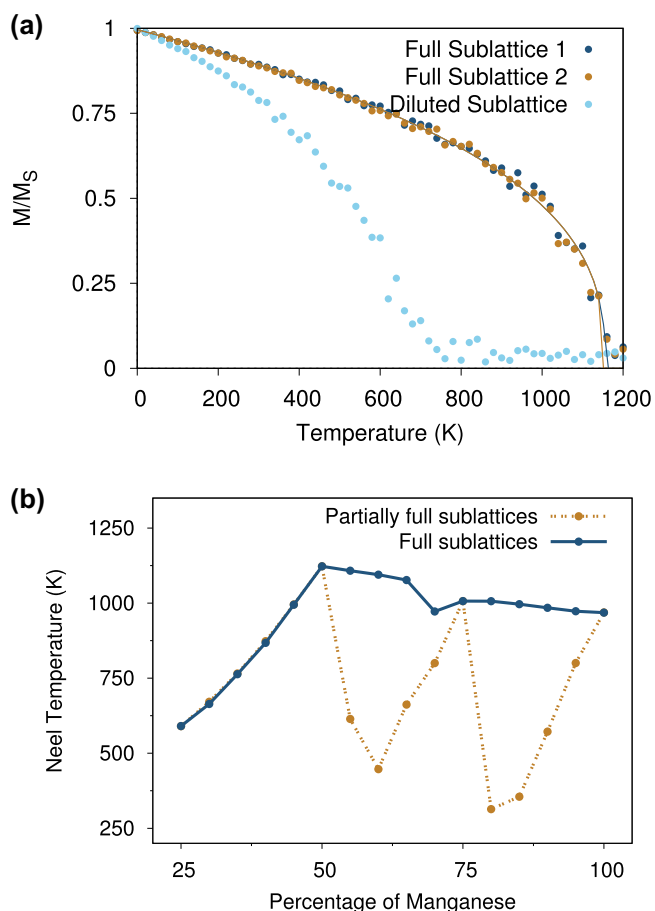
TABLE V. The percentage of magnetic Mn atoms in each sublattice for disordered IrMn as the percentage of Mn was increased from 25% to 100%.

Composition	Subblatice 1	Sublattice 2	Sublattice 3	Sublattice 4
$Ir_{75}Mn_{25}$	25	25	25	25
$Ir_{70}Mn_{30}$	30	30	30	30
$Ir_{65}Mn_{35}$	35	35	35	35
$Ir_{60}Mn_{40}$	40	40	40	40
...	:	:	:	:
$Ir_{15}Mn_{85}$	85	85	85	85
$Ir_{10}Mn_{90}$	90	90	90	90
Ir_5Mn_{95}	95	95	95	95
Mn_{100}	100	100	100	100

until completely full. Unlike for a fixed composition, the change in Néel temperature for intermediate ordered phases is caused by an increase in the angle between the sublattices as ($E \propto \cos(\theta)$), increasing the ground-state exchange energy due to geometric frustration. In the only partially ordered states, the angle between the sublattices (θ) must be smaller and therefore the Néel temperature decreases.

B. Néel temperatures of disordered Ir_xMn_{x-1} alloys

$IrMn_3$ is the most widely theoretically studied composition of IrMn. However, in most spintronic devices, the composition of IrMn used is not $IrMn_3$ but closer to $IrMn_4$ or $IrMn_5$ [47]. In the next section, the composition dependence of disordered iridium manganese is investigated, especially in the compositions between $IrMn_5$ to $IrMn_3$. The percentage of Mn was varied from 25% to 100% as outlined in Table V.

The Néel temperatures for the simulated disordered compositions are shown in Fig. 13. The simulations give a T_N of 1000 K for Mn. Neutron scattering measurements [12] calculate the T_N of Ir_0Mn_{100} to be much lower. The

FIG. 12. An example magnetization versus temperature curve for a partially ordered IrMn alloy and the simulated Néel temperatures against percentage of manganese. (a) Magnetization versus temperature curve for an Mn concentration of 65%. The partially filled sublattice has a much lower Néel temperature than the full sublattices but the magnetization length at zero Kelvin is still one. (b) The Néel temperature with percentage of Mn. The partially filled sublattices have been plotted separately as they have a much lower Néel temperature.

reach a saturation state at zero temperature. This is true for all of the compositions simulated. The lower Néel temperature for the diluted sublattice means it is hard to quantify the Néel temperature of the bulk material to a single value. The simulated Néel temperatures for all the compositions studied are shown in Fig. 12(b). The Néel temperatures have been plotted separately for the average of the full sublattices and for the diluted sublattice. These values are different for Mn values above 50%, however, below 50% the partially full sublattice has the same Néel temperature as the full sublattice. Below 50%, there is only one full sublattice, when the atoms are added in the next sublattice are added there is therefore no frustration between competing sublattices—they are just anti-ferromagnetically coupled to the first sublattice. This means even if only a few atoms are added, they are all strongly magnetized along the same direction. The Néel temperature of the full sublattices decreases almost linearly between the fully ordered states. The Néel temperature of the partially full sublattices increases as the percentage of Mn increases
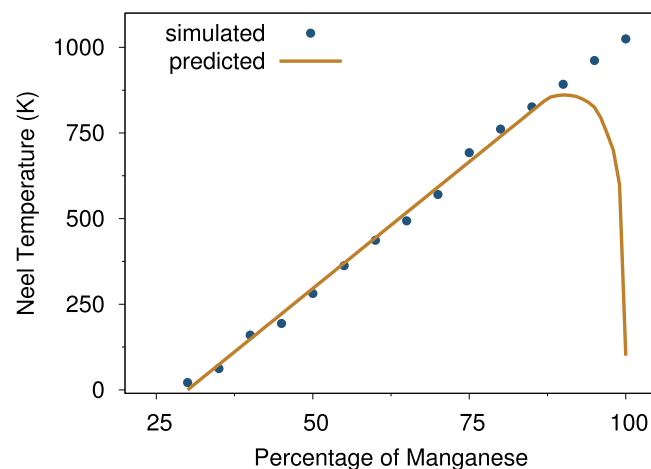

FIG. 13. The simulated and predicted Néel temperatures for disordered IrMn with different percentages of Mn. The simulated Néel temperatures increase linearly with Mn concentration but the prediction from previous experimental results is for the Néel temperature to decrease as the Mn concentration approaches 100%.
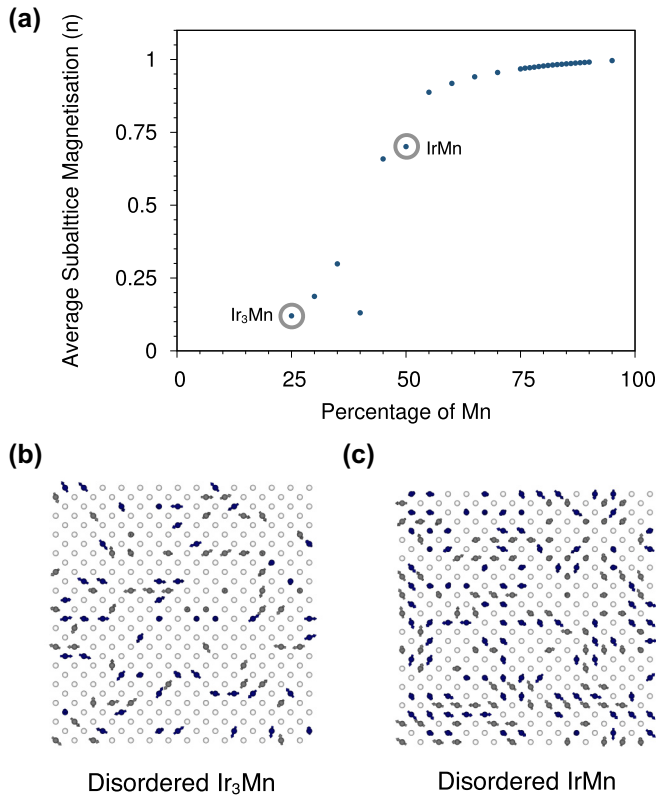
(a)

(b)   **(c)**

Disordered Ir_3Mn Disordered IrMn

FIG. 14. Average sublattice magnetization lengths (n) for disordered IrMn with different Mn compositions and interface magnetic structure for disordered Ir_3Mn and IrMn at $T = 0$ K. (a) The average sublattice magnetization length for different Mn compositions. The magnetization length is nearly one for all Mn percentages higher than 50% but for low concentrations the average sublattice magnetization is less than 30%. The magnetization structures for disordered (b) Ir_3Mn and (c) IrMn. Both compositions have almost zero net magnetization and form spin-glass structures.

discrepancy is due to the simulations, assuming the unit cell size and magnetic structure is constant for all compositions and orderings of IrMn whereas, in reality, for compositions greater than 95% Mn the system has a complex anisotropic structure [36]. At compositions greater than 95%, there is therefore a breakdown in the assumptions of the model and the results of our simulations are no longer accurate. The ordered compositions of IrMn have a higher Néel temperature than the disordered structures because of the increased frustration in the disordered systems. The frustration decreases the anisotropy causing the structures to be less stable. In fact, the simulations with a percentage of Mn atoms <25% have a low Néel temperature—almost zero.

To investigate why the Néel temperatures are so low for low percentages of Mn, the magnetization length was plotted for the different simulations and is shown in Fig. 14(a). For percentages of Mn above 75%, the average sublattice magnetization length is above 95%. For very high percentages of Mn > 0.8, the average sublattice magnetization length is above 99%, suggesting every atom in every sublattice is nearly perfectly aligned. The compositions used in hard drives (~18–24% Mn) have a higher degree of magnetic ordering than $IrMn_3$. For low percentages of Mn (less than 50%),

the average sublattice magnetization length is very low as the structure forms a spin glass because the concentration of Mn atoms is too low for a regular spin network to form. A cross section of the ground-state structure of IrMn and Ir_3Mn are shown in Fig 14(b). These show that the system has no long-range magnetic ordering explaining the low values of the Néel temperature for compositions with a low percentage of Mn atoms. Due to the spin-glass nature, the exact values of the local Néel ordering temperature will be inaccurate for compositions less than 60%, but naturally reflect the loss of long-range AFM order. An interesting application of the IrMn spin-glass system may be as a high temperature AFM spin glass [48–50] with ordering temperatures much closer to room temperature. This could enable new applications in brain-inspired computing and complex networks, with readout possible using the exchange bias effect.

In disordered $IrMn_3$, the ground-state spin structure is the 3Q tetragonal structure, characterized by an angle of 109.5° between the four magnetic sublattices. The ground-state structures of other compositions has so far never been theoretically studied even though in most hard drives compositions of 18–24% Ir are used. Usually, it is assumed that the magnetization structure is the same as $IrMn_3$ for all these compositions. By calculating the angle between the sublattices, we can see if this assumption is true. The angles between the sublattices are shown for Mn concentrations from 55–95% in Fig. 15(a). For all concentrations, the average angle between sublattices is 109.5°. The error in the angle is around 1% for all compositions between 18–24% Ir. From the angles, we can confirm that the compositions used in spintronic devices will also exhibit the 3Q structure shown in Fig. 15(b).

VI. MAGNETIC ANISOTROPY OF IrMn ALLOYS

The magnetic anisotropy of AFMs plays a key role in the stability of many spintronic devices, ensuring the thermal stability of AFM grains responsible for the exchange bias effect. The anisotropy of IrMn has previously been studied both experimentally and theoretically. The ordered phase of $IrMn_3$ was studied theoretically by Szunyogh *et al.* [15] using *ab initio* methods. They found an extremely large value for the second-order magnetic anisotropy, leading to energy barriers of the order of 3×10^7 J/m^3 at $T = 0$ K. This is an extraordinarily large value for the anisotropy. For comparison, neodymium iron boron is the strongest permanent magnet available today and has an anisotropy of 1.33×10^6 J/m^3: more than an order of magnitude smaller.

Vallejo-Fernandez *et al.* experimentally determined the anisotropy constant of disordered $IrMn_3$ by measuring the mean blocking temperature of a IrMn/CoFe bilayer [43,51]. The blocking temperature was measured using a training-free measurement procedure in which hysteresis loops were repeatedly measured at the same (thermal activation free) low-temperature after raising the sample to a different activation temperature. The activation reverses part of the AFM layer due to the exchange field from the FM. As the AFM reverses, the exchange bias field decreases and the blocking temperature (T_B) is the point where the exchange bias field is reduced to zero and was measured to be $T_B = 236$K. The blocking temperature is low because of the thin films they used (3 nm)
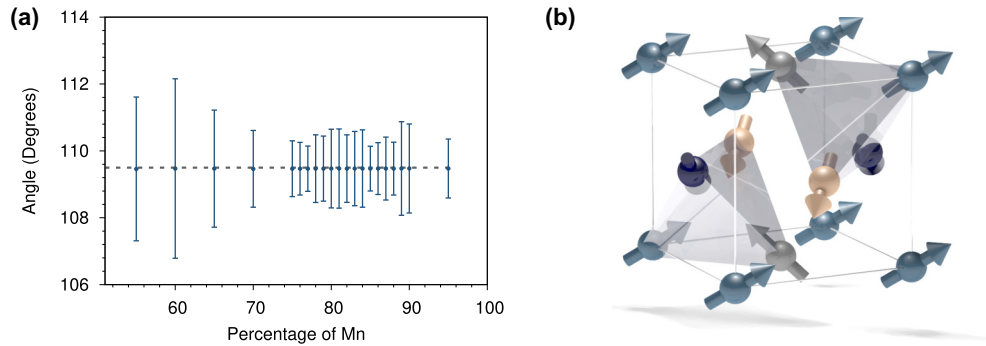
FIG. 15. Average angle between sublattices for disordered IrMn compositions and the ground-state magnetic structure of all the compositions. (a) The average angle between magnetic sublattices is 109.5° for all percentages of Mn higher than 50%. The error is the standard deviation in the angles. (b) All the compositions higher than 50% Mn concentration have therefore formed the same magnetic structure as $IrMn_3$.

and, using this value, the anisotropy can be determined given the measured grain volume using the equation

$$\tau^{-1} = f_0 \exp\left(-\frac{\Delta E}{k_B T}\right), \tag{8}$$

where τ is the relaxation time, ΔE is the energy barrier, k_B is the Boltzmann constant, and T is the temperature. At the blocking temperature $\Delta E = K_{AFM}V$, where K_{AFM} is the anisotropy constant of the AFM and V is the mean grain volume. The anisotropy constant is therefore given by

$$K_{AFM}(T_B) = \frac{\ln(\tau f_0)}{V} k_B T_B. \tag{9}$$

Using Eq. (10), the temperature variation can be calculated. The assumption is made that $l = 3$, which is only valid for a uniaxial magnetocrystalline anisotropy [44]. In combination with the Curie-Bloch equation in the classical limit [31], the temperature variation of the anisotropy can be described by the equation

$$K_{AFM}(T) = K_{AFM}(0)\left[\left(1 - \frac{T}{T_N}\right)^{0.34}\right]^3 \approx K_{AFM}(0)\left(1 - \frac{T}{T_N}\right). \tag{10}$$

At $T = 300\,\text{K}$ $K_{AFM} = 6.2 \times 10^5\,\text{J/m}^3$ and by extrapolation at $T = 0\,\text{K}$ $K_{AFM} = 14.8 \times 10^5\,\text{J/m}^3$, where the zero Kelvin value is almost two orders of magnitude lower than the theoretical calculations for ordered $IrMn_3$ [15]. The experimental measurement of the anisotropy constant is also dependent on the value of the switching attempt frequency (f_0). Originally, Vallejo-Fernandez et al. used a value of $f_0 = 10^9\,\text{s}^{-1}$ [43] but more recent estimates suggest values closer to $f_0 = (2.1 \pm 0.4) \times 10^{12}\,\text{s}^{-1}$ [52].

The symmetry of the anisotropy is also an unresolved problem. Vallejo-Fernandez [43] and Craig et al. [53] investigated the form of the anisotropy energy surface by fitting to the temperature dependence of the magnetization using a Callen-Callen [44] power law,

$$\frac{K_{AFM}(T)}{K_{AFM}(0)} = \left[\frac{n_{AFM}(T)}{n_{AFM}(0)}\right]^l, \tag{11}$$

where n_{AFM} is the AFM sublattice magnetization and l is an exponent which reflects the symmetry of the anisotropy. In materials with a uniaxial anisotropy, $l \sim 3$ and, for a cubic anisotropy, $l \sim 10$. The symmetry of the anisotropy generally reflects that of the lattice. While the Callen-Callen theory [44] holds for most FM materials because the anisotropy of AFM materials is so difficult to measure, it has previously been difficult to say if it will also hold for AFM materials. The theory will be tested for a AFM with a known symmetry to see if the temperature dependence is consistent with the Callen-Callen theory. Szunyogh et al. [15] calculated the energy surface for ordered $IrMn_3$ by rotating the triangular ground state around the (111) direction and calculating the change in energy. The same calculation was done using our IrMn model with the Néel pair anisotropy, in Fig. 8, finding an exact match to the ab initio results. Both experiment and theory agree that the anisotropy has a uniaxial form contradicting the predicted relationship between crystallographic symmetry and the temperature dependence of the anisotropy from the Callen-Callen [44] and Zener [54] relations. As IrMn has a cubic crystal structure, the anisotropy would normally be expected to have a cubic symmetry.

A. Constrained Monte Carlo

The energy barrier separating two ground states is the minimum energy path for the spins to rotate from one ground state to another. At a finite temperature, the anisotropy constant is a free-energy difference arising from spin fluctuations. To calculate the energy barrier, we use a constrained Monte Carlo (CMC) algorithm to determine the entire energy surface. From the energy surface, we can find the ground-state spin structures and calculate the minimum energy required to rotate between them. The CMC algorithm constrains the magnetization of one sublattice along a direction (θ, ϕ), while the other sublattices are unconstrained and free to evolve using a standard Monte Carlo sampling algorithm. Due to this constraint, the system is not in its ground state, causing a small restoring torque on the system. CMC [28] is an extension of the metropolis Monte Carlo algorithm where the steps of the random walk are modified to conserve the average
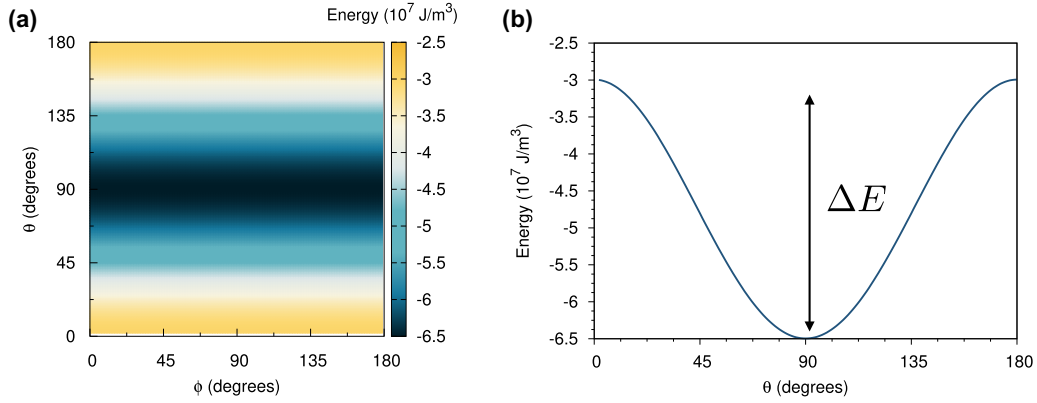
FIG. 16. Simulated anisotropy energy surface for $L1_0$-IrMn and the azimuthal angle dependence of the free energy. (a) The simulated energy surface calculated from the integral of the torque. It has the usual uniaxial symmetry. (b) The minimum energy path for a spin to rotate from the $+z$ to $-z$ directions. The easy plane anisotropy energy ΔE is shown.

magnetization direction ($\hat{\mathbf{M}}$) as

$$\hat{\mathbf{M}} \equiv \frac{\sum_i (\hat{\mathbf{S}}_i)}{\| \sum_i \hat{\mathbf{S}}_i \|}, \qquad (12)$$

where $\mathbf{S}_i$ is the unit vector of the direction of magnetization of a spin i. The constraint keeps the system out of equilibrium in a controlled manner but allows its microscopic degrees of freedom to thermalize [28]. The energy surface is calculated by constraining the direction of magnetization of a single sublattice of the AFM along a specific (θ, ϕ) direction while allowing all other spins in the system to equilibrate to a minimum energy state. The constraint used is a weaker constraint than that used by Szunyogh *et al.* where all of the sublattices were rigidly constrained preserving $120°$ between each sublattice. The constrained sublattice spins are integrated using using a CMC algorithm while the other sublattice spins are integrated using a regular Monte Carlo algorithm. For each value of θ and ϕ, the system was initially heated to 1500 K to thermalize the spins and then cooled to 0 K. The simulation was run over 1 000 000 MC steps to the ground state for each θ, ϕ value, using batch parallelization for each unique angle pair.

The CMC method determines the Helmholtz free energy ($\mathscr{F}$) for a given constraint direction. This cannot be computed directly but is related to the internal energy (E) as

$$\mathscr{F} = E - TS, \qquad (13)$$

where T is the temperature and S is the entropy. At zero Kelvin, the internal energy equals the Helmholtz free energy ($\mathscr{F}$). The internal energy can be calculated directly as the sum of all the energies acting on the system (anisotropy, dipolar, exchange, etc.) but we cannot calculate the entropy S without doing work on the system. Instead $\mathscr{F}$ can be indirectly calculated from the integral of the torque (τ) acting upon the system.

The magnetic torque can be defined as

$$\tau = \langle \mathbf{M} \rangle \times \langle \mathbf{B} \rangle, \qquad (14)$$

where $\mathbf{M}$ is the average magnetic moment and $\mathbf{B}$ is the average magnetic field acting on this moment. The torque is a measure of the force that can cause an object to rotate about an axis

and, in this case, causes a precession of the magnetic moment around the effective field. Our system is comprised of many atoms all with their own individual moment $\mathbf{S}_i$ In our system, the field is defined by $\mathbf{B}_i = -\partial \mathscr{H} / \mu_S \partial \mathbf{S}_i$ and the total torque is given by

$$\tau = -\langle \mathbf{M} \rangle \times \frac{\partial \mathscr{F}}{\partial \mathbf{M}}, \qquad (15)$$

where $\mathbf{M}$ is the magnetization direction and $\mathbf{M} = \sum_i \mathbf{S}_i$, where $\mathbf{S}_i$ is the direction of spin i. The Helmholtz free energy cannot be computed directly and so instead we can reconstruct it from the integral of the torque,

$$\Delta \mathscr{F} = \mathscr{F}(\mathbf{M}_0) + \int_{\mathbf{M}_0}^{\mathbf{M}} (\mathbf{M}' \times \tau) \cdot d\mathbf{M}', \qquad (16)$$

where the integral of the torque is taken along the minimum energy path between two points ($\mathbf{M}_0$ and $\mathbf{M}$) on the energy surface along states $\mathbf{M}'$. From this, the energy barrier to magnetic reversal can be calculated. At zero Kelvin, the energy to rotate between these ground states ($\mathscr{F}$) equals the internal energy (E), but at higher temperatures this is not the case and the free energy must be calculated from the torque.

B. The anisotropy in ordered $L1_0$-IrMn

From the crystal symmetry, $L1_0$ ordered IrMn has an easy plane magnetization, shown in Fig. 11(c). In the following section, we will calculate the energy barrier to magnetic reversal from the torque and then determine the scaling of the anisotropy compared to the temperature dependence of the magnetization. As IrMn has uniaxial symmetry, we expect the temperature dependence to give a uniaxial exponent of $l = 3.0$ in the Callen-Callen relation in Eq. (11).

A 8 nm $\times$ 8 nm $\times$ 8 nm system of $L1_0$-ordered IrMn was simulated and a full energy surface was created by running a CMC simulation with the magnetization of one of the sublattices constrained along a θ, ϕ direction. θ, ϕ were incremented in $1°$ steps and at each step a simulation was run for 3 000 000 Monte Carlo steps. The first 1 000 000 steps of the simulation were equilibration steps, meaning the calculated energy/torque values did not contribute to the final average energy/torque values. During the equilibration time
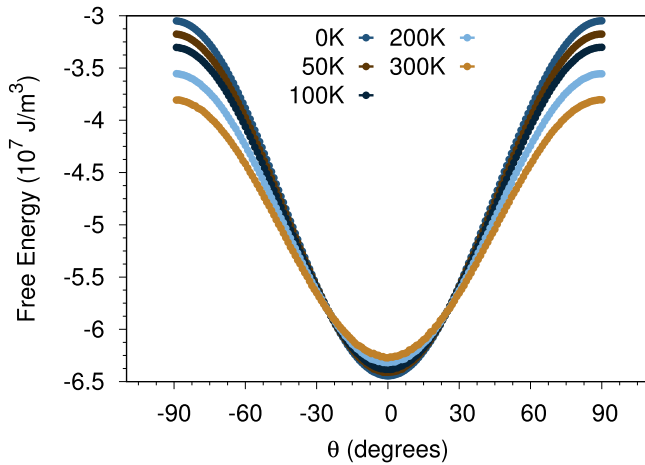
FIG. 17. The temperature dependence of the anisotropy in L1$_2$-IrMn. The minimum energy path between ground states for temperatures of 0 K, 10 K, 100 K, and 300 K.

FIG. 18. The scaling of the effective energy barrier with sublattice magnetization length n_{AFM} fitted using $E_B(n_{\text{AFM}}) = E_0 n^l_{\text{AFM}}$. l is calculated to be $l = 3.0005 \pm 0.0002$, suggesting a scaling similar to uniaxial anisotropy $l = 3$.

steps, the system should find its minimum energy state so the output average free energy/torque values only include the equilibrated free energy.

The energy surface produced is shown in Fig. 16, where the minimum energies occur when $\theta = 90°$ and the maximum energy occurs when $\theta = 0°, 180°$. The easy-plane anisotropy found agrees with the *ab initio* results of Szunyogh *et al.* [15] and Umetsu *et al.* [55] and experimental measurements [45]. The energy barrier is calculated as the difference between the maximum and minimum energies. For our simulation, this gave a large value of 3.49×10^7 J/m^3, larger than the *ab initio* values calculated by Szunyogh *et al.* (1.78×10^7 J/m^3) and Umetsu *et al.* (2.07×10^7 J/m^3) for the L1$_2$ phase and an order of magnitude larger than the value calculated by Vallejo-Fernandez *et al.* for the γ phase. The discrepancy with the *ab initio* values arises due to the missing small lattice relaxation in our simplified model which is parameterized for the L1$_2$ phase.

The temperature dependence of the anisotropy energy barrier is calculated by running the same simulation as described to create Fig. 16 but at increasing temperatures. Previously, the simulation was run over all θ, ϕ angles, however, as we now know, for the minimum energy path only the θ, $\phi = 0$ values along this path were simulated. The simulation was run through exactly the same simulation steps but repeated at increasing temperatures. The temperatures were increased in 10 K intervals between 0 K and 300 K. The energy barrier was calculated from the torque again and the energy barriers at 0 K, 10 K, 100 K, and 300 K are shown in Fig. 17. The total energy of the system has increased with temperature but the energy barrier (ΔE) has decreased due to thermal fluctuations.

The exponent (l) is calculated by plotting the scaling of the anisotropy energy barrier with sublattice magnetization length n_{AFM} on a logarithmic scale. Figure 18 shows the result, giving a temperature dependence of $l = 3.0004 \pm 0.0003$. The exponent almost exactly matches a uniaxial exponent suggesting that the Callen-Callen law applies for AFM materials as well as FM materials provided the lattice has appropriate symmetry. Previously, it has been thought that the Callen-Callen
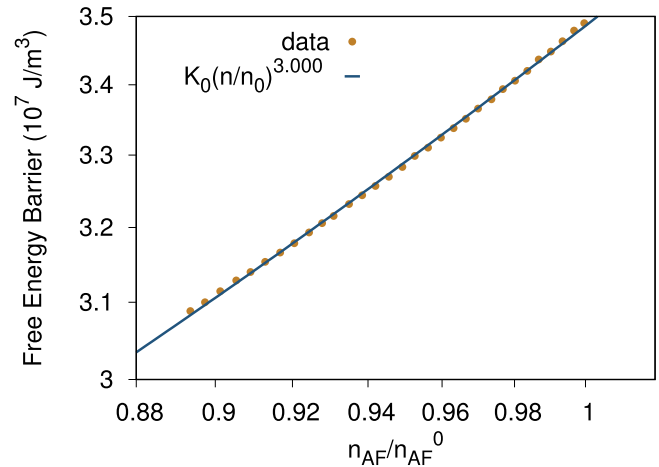
law does not apply to AFMs [44] and that they would have different scaling laws than FM materials. However, here it has been proven that an in-plane AFM follows the same scaling laws as an in-plane FM. In the next section, the anisotropy of IrMn$_3$ in both its ordered and disordered phases will be investigated. In these phases, the magnitude and symmetry of the anisotropy is a more complex question to address.

C. The anisotropy in ordered L1$_2$-IrMn$_3$

In ordered L1$_2$-IrMn$_3$ the ground state occurs when the magnetic moments lie in-plane perpendicular to the (111) crystal direction with the three sublattice magnetizations oriented 120° apart. By symmetry, a cube contains eight different (111) planes, meaning that ordered IrMn$_3$ actually contains eight different ground states corresponding to the 8 (111) planes. These ground states are all rotations of each other and are shown in Fig. 19. The positions of the energy minima can be predicted from the ground-state structures. For a single sublattice, the calculated minima are outlined in Table VI.

The simulated system was 8 nm × 8 nm × 8 nm. The zero Kelvin energy surface is shown in Fig. 20 and has a
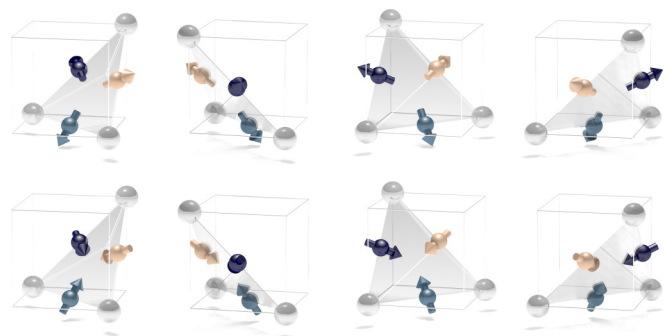

FIG. 19. The eight possible ground-state magnetic structures in ordered IrMn$_3$ corresponding to the eight (111) planes. The (111) planes are outlined via the pale grey triangles in the image.

TABLE VI. The eight possible ground-state magnetization directions for one sublattice of IrMn, each of the other two sublattices will have their own eight minima.

Direction	θ	ϕ
(0.83, 0.39, 0.39)	25	67
(−0.83, 0.39, 0.39)	155	67
(−0.83, −0.39, 0.39)	205	67
(0.83, −0.39, 0.39)	335	67
(0.83, 0.39, −0.39)	25	113
(−0.83, 0.39, −0.39)	155	113
(−0.83, -0.39, −0.39)	205	113
(0.83, -0.39, −0.39)	335	113

complicated structure with eight minima. The figure only shows four of the eight ground states due to symmetry. The energy minima lie at $\phi \sim 67°$, $113°$, and $\theta \sim 155°$, $205°$, corresponding to the expected easy directions of the constrained sublattice in Table VI.

To calculate the energy barrier between two adjacent minima, we compute the minimum energy path between them. The minimum energy path is outlined as the white line in Fig. 20 and the energy of this line is shown in Fig. 21. The calculated 0 K energy barrier is 1.78×10^6 J/m^3, and an order of magnitude lower than that calculated by Szunyogh *et al.* [15] for a rigid spin rotation around the (111) plane. This has massively reduced the disparity between the experiment and theory, with this result being only 20% more than the experimental measurement.

The reduction in the energy barrier compared to the previous theoretical results arises due to a small bobbing motion of the unconstrained spins. The bobbing results from the competition between the exchange and anisotropy energies leading to small deviations from the ground-state spin structure when the AFM spins are rotated between energy minima. The reduction in energy barrier can be observed because our model has used a weaker constraint than Szunyogh *et al.* [15].
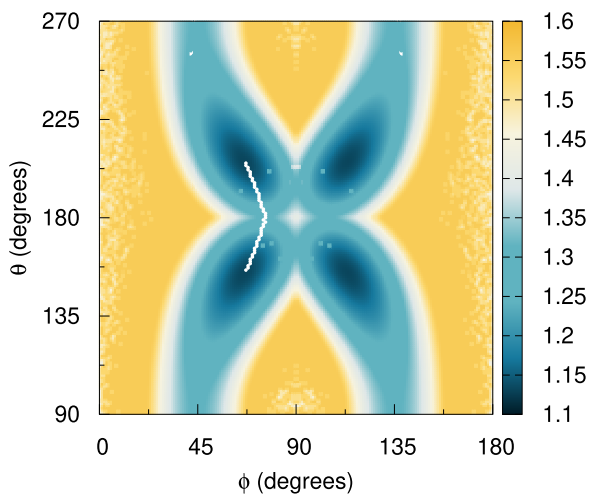

FIG. 20. Simulated anisotropy energy surface for ordered L1$_2$-IrMn$_3$ at 0 K. This was calculated from the integral of the total torque. The marked path shows the minimum energy route between the two energy minima.
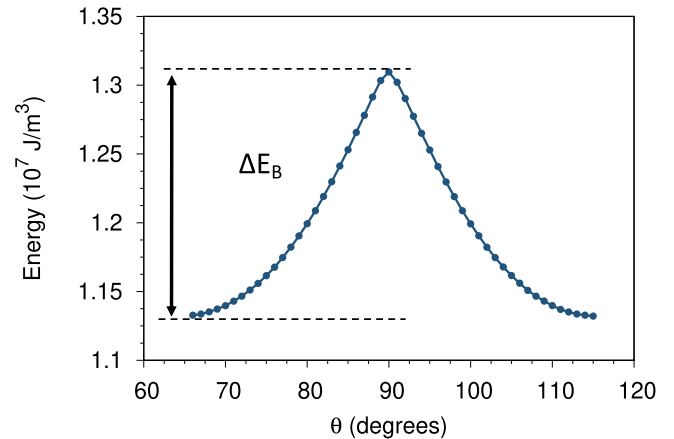

FIG. 21. Cross section of the anisotropy surface at $T = 0$ K showing the minimum energy path to reversal between two ground states for L1$_2$-ordered IrMn$_3$. The energy barrier ΔE_B to move between the minima is shown.

This result is particularly relevant to macroscopic approximations of AFM materials with Néel vectors where the sublattices are always assumed to have a fixed local spin structure. The remaining difference in the values of the effective magnetic anisotropy could be due to different ordering or defects in the experimental samples, but our results finally resolve the large disparity between the theoretically calculated and experimentally measured magnetic anisotropy of IrMn$_3$ [34]. We note that, although the energy surface illustrated in Fig. 20 has an unusually complex form, the minima themselves exhibit a fourfold symmetry, characteristic of cubic rather than uniaxial anisotropy. The question remains how to resolve the apparent contradiction with the experimental data of Vallejo-Fernandez *et al.* [43] and its requirement of a magnetization scaling exponent $l = 3$ consistent with uniaxial symmetry.

To resolve this discrepancy, we now investigate the temperature dependence of the anisotropy constant to calculate the scaling exponent. The energy surfaces and minimum energy path were calculated for temperatures between 0 K and 350 K as shown in Fig. 22. The absolute free energy increases with temperature due to spin fluctuations but the free energy barrier between neighboring ground-state minima, i.e., the magnetic anisotropy, decreases. In Fig. 22, we plot the power-law dependence of the effective energy barrier as a function of the magnetization and find an unusual exponent of $l = 3.92 \pm 0.14$. The exponent is closer to a uniaxial exponent of $l = 3$, matching the experimental observations, but deviates from this ideal value due to the complex symmetry of the anisotropy energy surface. We also note that the specific scaling exponent is dependent on the strength of the anisotropy, and for weaker anisotropy tends toward an exponent of $l = 3$, which may be seen in similar noncollinear magnets such as PtMn$_3$. We conclude that the magnetic anisotropy of L1$_2$- IrMn$_3$ possesses a close to uniaxial temperature dependence in direct contradiction with the usual Callen-Callen power laws and cubic nature of the crystal [44]. However, the uniaxial symmetry is consistent with the symmetry of the local energy surface of individual atoms in the crystal as the spin fluctuations are taking place in a uniaxial environment.
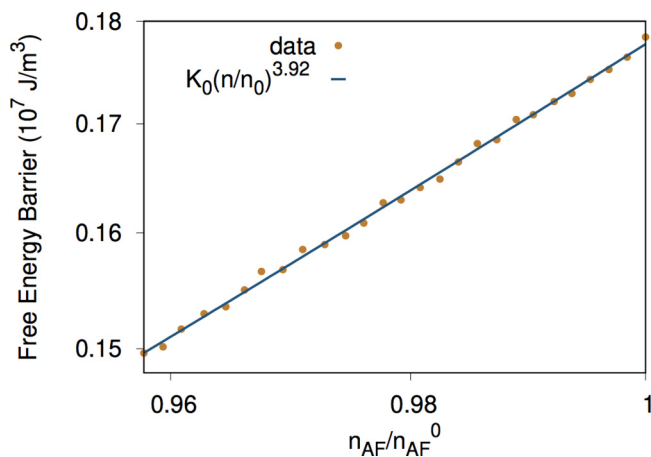
FIG. 22. The scaling of the effective energy barrier with sublattice magnetization length n_{AFM} fitted using $E_B(n_{AFM}) = E_0 n_{AFM}^l$. l is calculated to be 3.92 ± 0.14 suggesting a scaling similar to uniaxial anisotropy $l = 3$.

FIG. 23. Simulated anisotropy energy surface for disordered γ-IrMn$_3$ at 0 K. This was calculated from the integral of the total torque. The marked path shows the minimum energy route between the two energy minima.

D. Calculation of the anisotropy in disordered γ-IrMn$_3$

In the previous section, we calculated the symmetry and magnitude of the anisotropy in ordered L1$_2$-IrMn$_3$ and compared it to the experimental energy barrier. However, the experimental measurements typically use a disordered alloy of IrMn close to IrMn$_3$. In the following section, the energy barrier is calculated for disordered IrMn$_3$ with the aim of reducing the disparity with experimental results.

In disordered IrMn$_3$, the ground state occurs when the spins in each sublattice are oriented 109.5° apart in a tetragonal structure. As with ordered IrMn$_3$ there are eight ground states corresponding to the eight (111) planes. These ground states are all rotations of each other as with ordered IrMn$_3$ shown in Fig. 19.

The energy surface was computed using the same method as the previous two sections using a 8 nm × 8 nm × 8 nm system. The zero Kelvin energy surface is shown in Fig. 23. The energy surface has a remarkably cubic symmetry, which is a reflection of the lattice. There are four energy minima in the diagram located at $\phi \sim 55°$, 125°, and $\theta \sim 45°$, 135°. The disordered IrMn$_3$ energy surface has four clear minima, however, the maxima show a lot of noise which comes from the natural disorder in the structure.

The minimum energy path between two adjacent ground states is outlined in Fig. 23 as a white line. The line shows more noise fluctuations in comparison to that of ordered IrMn$_3$ due to the noise in the energy surface. The energy along the path is shown in Fig. 24. The energy barrier has a much smoother transition between energy states than would be expected from the energy surface. The shape of the energy barrier is very similar to that of ordered IrMn$_3$ but the energy difference is slightly lower at only 9.96×10^5 J/m^3. The value is 40% lower than the experimentally measured value from Vallejo-Fernandez *et al.* but as with ordered IrMn$_3$ the value has greatly reduced from previous theoretical calculations. The remaining difference between our value and the experimental value could be due to differences in composition. We have used IrMn$_3$ however often the composition used
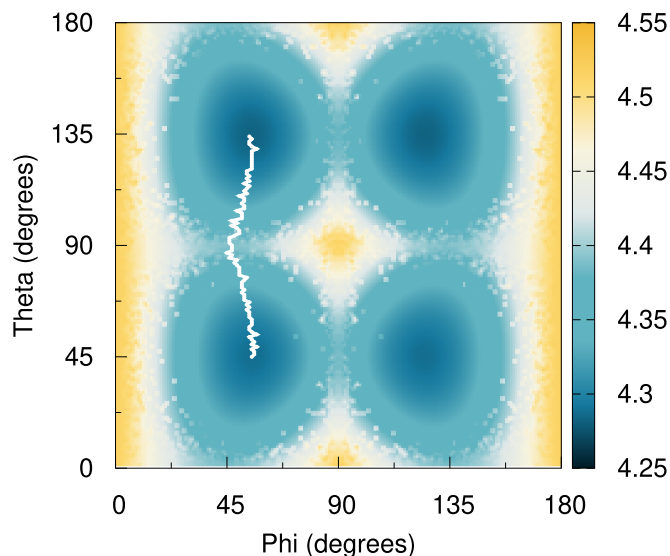
experimentally is closer to IrMn$_4$, which may alter the total anisotropy for the material.

The energy surface shows a distinctly cubic symmetry, and as for the ordered L1$_2$-IrMn reflects the cubic nature of the crystal. The temperature dependence of the sublattice magnetization was calculated for disordered IrMn$_3$ as in the previous two sections. The result is shown in Fig. 25 and the Callen-Callen exponent was calculated to be 3.12 $\pm$ 0.03. The temperature dependence is only 4% off the uniaxial exponent. The result is surprising due to the clear cubic symmetry in the energy surface. The apparent contradiction is again due to the local energy surface felt by each atom. The energy surface is cubic, however, each individual spin sits in a uniaxial-like energy surface. The local environment for each spin governs the spin fluctuations rather
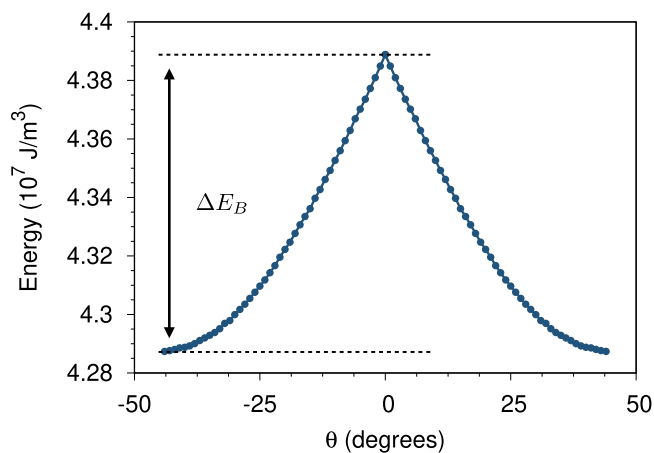

FIG. 24. Cross section of the anisotropy surface at $T = 0$ K for $\gamma - $IrMn$_3$ showing the minimum energy path to reversal between two ground states. The energy barrier ΔE_B to move between the minima is shown.
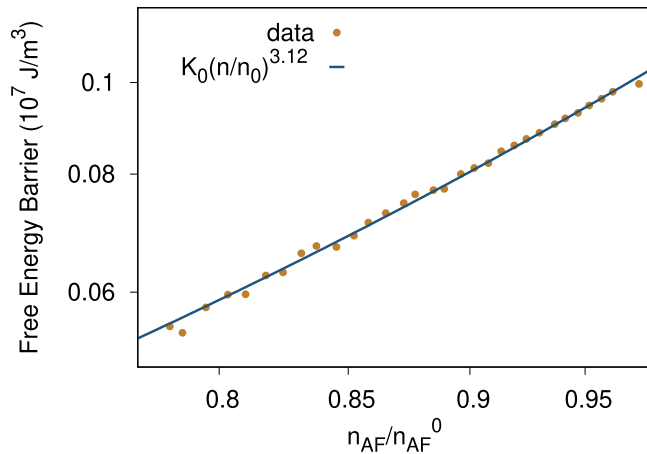
FIG. 25. The scaling of the effective energy barrier with sublattice magnetization length n_{AFM} for γ-IrMn$_3$ fitted using $E_B(n_{AFM}) = E_0 n_{AFM}^l$. l is calculated to be 3.12 ± 0.03, suggesting a scaling similar to uniaxial anisotropy $l = 3$.

than the symmetry of the energy surface as a whole. The results go a long way toward understanding the large difference between the previous experimental and theoretical results. In particular, comparing our findings with experimental measurements suggests that the exceptionally large value of the anisotropy calculated by Szunyogh *et al.* may well be an underestimate, with experimental measurements predicting larger values of the anisotropy. A further effect not considered in our present model is the importance of two-ion anisotropy from anisotropic exchange interactions [15] which show a weaker temperature dependence than single-ion contributions [56]. In addition, quantum effects in the temperature dependence of the magnetization may also be important, particularly for the ordered phases, which may reduce the effects of thermal fluctuations [31] and thereby reduce the temperature dependence of the anisotropy. The combination of these effects may reduce the need to increase the value of the anisotropy constant beyond the *ab initio* value, but will require more extensive experimental measurements and an adaptation of the Néel pair anisotropy to include contributions that are two-ion in nature. Despite the limitations, our model is able to reproduce the fundamental anisotropies and temperature dependencies of ordered and disordered IrMn alloys in close agreement with experimental measurement.

Given the differing anisotropy scaling exponents for the different phases of IrMn, it is useful at this point to consider the physical origins and if such effects may be seen in other systems. With the exception of the L1$_0$-IrMn phase, the calculated exponents do not agree with the usual Callen-Callen exponents because of the frustrated exchange interactions between the different sublattices. In FMs, ferrimagnets, and collinear AFMs, small thermal spin fluctuations retain a net average direction that is almost perfectly aligned with the minimum energy direction defined by the anisotropy, be it uniaxial or cubic in nature. For noncollinear AFMs with very large anisotropy, this alignment is broken, as the preferred lo-

cal spin directions are constrained by the frustrated exchange interactions, and so the local anisotropy energy minimum and total energy minimum no longer align. Thus, small thermal deviations of the spin directions leads to an additional contribution to the energy due to exchange but whose symmetry is different from the local magnetic anisotropy. We expect that the unusual scaling exponents are therefore a unique property of noncollinear AFMs, and that the exponent converges toward the Callen-Callen scaling for weaker anisotropy since the exchange becomes more dominant and so the average direction of the noncollinear spins aligns more with the global energy minimum.

VII. CONCLUSION

In conclusion, we have presented a unifying atomistic model of Ir$_x$Mn$_{1-x}$ alloys, reproducing the broad physical characteristics of this fascinating and complex magnetic material. In Mn-rich compositions, the material is AFM with a high magnetic ordering (Néel) temperature and very large magnetocrystalline anisotropy, with collinear and T1 and 3Q noncollinear spin structures. In Mn-poor concentrations, it exhibits FM ordering for the L1$_0$-Ir$_3$Mn ordered phase and spin-glass behavior in the γ phase, both with ordering temperatures at or above room temperature. The Néel temperature is predicted to increase with Mn concentration within the approximations of our model, allowing broad tunability based on composition and crystallographic ordering. In general, the magnetic anisotropy possesses a symmetry based on the underlying lattice symmetry but with a temperature dependence close to uniaxial for both ordered and disordered phases.

In some respects, this material system represents a true universal magnet, enabling fundamental studies of different kinds of magnetic ordering and dynamics simply by changing its composition and crystallographic ordering. It may represent one of the first high-temperature AFM spin-glass systems, enabling new applications in brain-inspired computing. The tunability of the effective magnetic properties such as Néel temperature, anisotropy, and collinearity allow precise engineering of magnetic properties to study the interaction of electrical currents with different classes of AFMs and develop functional AFM spintronic devices that work effectively at and above room temperature. Further experimental and theoretical studies will undoubtedly improve our understanding of IrMn as well as the accuracy of models of its static and dynamic properties.

[1] L. Néel, Magnetism and the local molecular field, Science **174**, 985 (1971).

[2] T. Jungwirth, X. Marti, P. Wadley, and J. Wunderlich, Antiferromagnetic spintronics, Nat. Nanotechnol. **11**, 231 (2016).

[3] T. Jungwirth, J. Sinova, A. Manchon, X. Marti, J. Wunderlich, and C. Felser, The multiple directions of antiferromagnetic spintronics, Nat. Phys. **14**, 200 (2018).

[4] R. Duine, Spintronics: An alternating alternative, Nat. Mater. **10**, 344 (2011).

[5] Y. Y. Wang, C. Song, B. Cui, G. Y. Wang, F. Zeng, and F. Pan, Room-Temperature Perpendicular Exchange Coupling and Tunneling Anisotropic Magnetoresistance in an Antiferromagnet-Based Tunnel Junction, Phys. Rev. Lett. **109**, 137201 (2012).

[6] M. B. Jungfleisch, W. Zhang, and A. Hoffmann, Perspectives of Antiferromagnetic Spintronics, Phys. Rev. Lett. A **382**, 865 (2018).

[7] S. Jenkins, A. Meo, L. E. Elliott, S. K. Piotrowski, M. Bapna, R. W. Chantrell, S. A. Majetich, and R. F. L. Evans, Magnetic stray fields in nanoscale magnetic tunnel junctions, J. Phys. D **53**, 044001 (2020).

[8] V. Saidl, P. Němec, P. Wadley, V. Hills, R. P. Campion, V. Novák, K. W. Edmonds, F. Maccherozzi, S. S. Dhesi, B. L. Gallagher, F. Trojánek, J. Kuneš, J. Železný, P. Malý, and T. Jungwirth, Optical determination of the Néel vector in a CuMnAs thin-film antiferromagnet, Nat. Photonics **11**, 91 (2017).

[9] L. Baldrati, A. Ross, T. Niizeki, C. Schneider, R. Ramos, J. Cramer, O. Gomonay, M. Filianina, T. Savchenko, D. Heinze, A. Kleibert, E. Saitoh, J. Sinova, and M. Kläui, Full angular dependence of the spin Hall and ordinary magnetoresistance in epitaxial antiferromagnetic NiO(001)/Pt thin films, Phys. Rev. B **98**, 024422 (2018).

[10] G. R. Hoogeboom, A. Aqeel, T. Kuschel, T. T. Palstra, and B. J. Van Wees, Negative spin Hall magnetoresistance of Pt on the bulk easy-plane antiferromagnet NiO, Appl. Phys. Lett. **111**, 052409 (2017).

[11] T. Yamaoka, Antiferromagnetism in γ-phase Mn-Ir alloys, J. Phys. Soc. Jpn. **36**, 445 (1974).

[12] I. Tomeno, H. N. Fuke, H. Iwasaki, M. Sahashi, and Y. Tsunoda, Magnetic neutron scattering study of ordered Mn_3 Ir, J. Appl. Phys. **86**, 3853 (1999).

[13] A. Kohn, A. Kovács, R. Fan, G. J. McIntyre, R. C. C. Ward, and J. P. Goff, The antiferromagnetic structures of $IrMn_3$ and their influence on exchange-bias., Sci. Rep. **3**, 2412 (2013).

[14] A. Sakuma, K. Fukamichi, K. Sasao, and R. Y. Umetsu, First-principles study of the magnetic structures of ordered and disordered Mn-Ir alloys, Phys. Rev. B **67**, 024420 (2003).

[15] L. Szunyogh, B. Lazarovits, L. Udvardi, J. Jackson, and U. Nowak, Giant magnetic anisotropy of the bulk antiferromagnets IrMn and IrMn3 from first principles, Phys. Rev. B **79**, 020403 (2009).

[16] K. O'Grady, L. E. Fernandez-Outon, and G. Vallejo-Fernandez, A new paradigm for exchange bias in polycrystalline thin films, J. Magn. Magn. Mater. **322**, 883 (2010).

[17] P.-H. Lin, B.-Y. Yang, M.-H. Tsai, P.-C. Chen, K.-F. Huang, H.-H. Lin, and C.-H. Lai, Manipulating exchange bias by spin–orbit torque, Nat. Mater. **18**, 335 (2019).

[18] S. Fukami, C. Zhang, S. Duttagupta, A. Kurenkov, and H. Ohno, Magnetization switching by spin-orbit torque in an antiferromagnet-ferromagnet bilayer system, Nat. Mater. **15**, 535 (2016).

[19] H. Ohldag, A. Scholl, F. Nolting, E. Arenholz, S. Maat, A. T. Young, M. Carey, and J. Stöhr, Correlation Between Exchange Bias and Pinned Interfacial Spins, Phys. Rev. Lett. **91**, 017203 (2003).

[20] W. Zhang, W. Han, S.-H. Yang, Y. Sun, Y. Zhang, B. Yan, and S. S. P. Parkin, Giant facet-dependent spin-orbit torque and spin Hall conductivity in the triangular antiferromagnet $IrMn_3$, Sci. Adv. **2**, e1600759 (2016).

[21] S. M. Rezende, J. B. S. Mendes, D. S. Maior, J. E. Abrão, A. Azevedo, and R. L. Rodríguez-Suárez, Magnon dispersion relations in the noncollinear antiferromagnet$IrMn_3$, Phys. Rev. B **102**, 054435 (2020).

[22] S. Jenkins, R. W. Chantrell, and R. F. L. Evans, Spin wave excitations in exchange biased IrMn/CoFe bilayers, J. Appl. Phys. **128**, 033903 (2020).

[23] S. Jenkins, W. J. Fan, R. Gaina, R. W. Chantrell, T. Klemmer, and R. F. L. Evans, Atomistic origin of exchange anisotropy in noncollinear γ-$IrMn_3$-CoFe bilayers, Phys. Rev. B **102**, 140404(R) (2020).

[24] S. Jenkins, R. W. Chantrell, and R. F. L. Evans, Exchange bias in multigranular noncollinear $IrMn_3$/CoFe thin films, Phys. Rev. B **103**, 014424 (2021).

[25] X. Zhou, L. Ma, Z. Shi, W. J. Fan, J.-G. Zheng, R. F. L. Evans, and S. M. Zhou, Magnetotransport in metal/insulating-ferromagnet heterostructures: Spin Hall magnetoresistance or magnetic proximity effect, Phys. Rev. B **92**, 060402(R) (2015).

[26] J. Zhou, X. Shu, Y. Liu, X. Wang, W. Lin, S. Chen, L. Liu, Q. Xie, T. Hong, P. Yang, B. Yan, X. Han, and J. Chen, Magnetic asymmetry induced anomalous spin-orbit torque in IrMn, Phys. Rev. B **101**, 184403 (2020).

[27] R. F. Evans, W. J. Fan, P. Chureemart, T. A. Ostler, M. O. Ellis, and R. W. Chantrell, Atomistic spin model simulations of magnetic nanomaterials, J. Phys.: Condens. Matter **26**, 103202 (2014).

[28] P. Asselin, R. F. L. Evans, J. Barker, R. W. Chantrell, R. Yanes, O. Chubykalo-Fesenko, D. Hinzke, and U. Nowak, Constrained Monte Carlo method and calculation of the temperature dependence of magnetic anisotropy, Phys. Rev. B **82**, 054415 (2010).

[29] J. D. Alzate-Cardona, D. Sabogal-Suárez, R. F. L. Evans, and E. Restrepo-Parra, Optimal phase space sampling for Monte Carlo simulations of Heisenberg spin systems, J. Phys.: Condens. Matter **31**, 095802 (2019).

[30] R. Evans, https://vampire.york.ac.uk/.

[31] R. F. L. Evans, U. Atxitia, and R. W. Chantrell, Quantitative simulation of temperature-dependent magnetization dynamics and equilibrium properties of elemental ferromagnets, Phys. Rev. B **91**, 144425 (2015).

[32] D. Hinzke, U. Nowak, and D. Garanin, Uniform susceptibility of classical antiferromagnets in one and two dimensions in a magnetic field, Eur. Phys. J. B **16**, 435 (2000).

[33] S. Jenkins and R. F. L. Evans, Enhanced finite size and interface mixing effects in iridium manganese ultra thin films, J. Appl. Phys. **124**, 152105 (2018).

[34] S. Jenkins, R. W. Chantrell, T. J. Klemmer, and R. F. L. Evans, Magnetic anisotropy of the noncollinear antiferromagnet IrMn3, Phys. Rev. B **100**, 220405(R) (2019).

[35] L. Szunyogh, L. Udvardi, J. Jackson, U. Nowak, and R. Chantrell, Atomistic spin model based on a spin-cluster expansion technique: Application to the IrMn$_3$/Co interface, Phys. Rev. B **83**, 024401 (2011).

[36] A. J. Bradley and J. Thewlis, The crystal structure of α-manganese, Proc. R. Soc. London, Ser. A **115**, 456 (1927).

[37] R. Y. Umetsu, M. Miyakawa, K. Fukamichi, and A. Sakuma, Pseudogap in the density of states and the highest néel temperature of the $L1_0$-type MnIr alloy system, Phys. Rev. B **69**, 104411 (2004).

[38] L. Neel, L'approche à la saturation de la magnétostriction, J. Phys. Radium **15**, 376 (1954).

[39] A. Akhiezer, V. G. Bar'yakhtar, and S. V. Peletminskii, *Spin Waves,* edited by S. Doniach (Amsterdam North-Holland Pub. Co., Amsterdam, 1968).

[40] M. Strungaru, S. Ruta, R. F. L. Evans, and R. W. Chantrell, Model of Magnetic Damping and Anisotropy at Elevated Temperatures: Application to Granular FePt Films, Phys. Rev. Applied **14**, 014077 (2020).

[41] R. Skomski, *Simple Models of Magnetism* (OUP, Oxford, 2008).

[42] R. Yanes, O. Chubykalo-Fesenko, H. Kachkachi, D. A. Garanin, R. Evans, and R. W. Chantrell, Effective anisotropies and energy barriers of magnetic nanoparticles with néel surface anisotropy, Phys. Rev. B **76**, 064416 (2007).

[43] G. Vallejo-Fernandez, L. E. Fernandez-Outon, and K. O'Grady, Measurement of the anisotropy constant of antiferromagnets in metallic polycrystalline exchange biased systems, Appl. Phys. Lett. **91**, 212503 (2007).

[44] H. Callen and E. Callen, The present status of the temperature dependence of magnetocrystalline anisotropy, and the l(l+1)2 power law, J. Phys. Chem. Solids **27**, 1271 (1966).

[45] K. Selte, A. Kjekshus, A. F. Andresen, and W. B. Pearson, Equiatomic transition metal alloys of manganese. VII. A neutron diffraction study of magnetic ordering in the IrMn phase., Acta Chem. Scand. **22**, 3039 (1968).

[46] D. M. K. Paul and W. G. Stirling, Magnetic excitations in Pt$_3$Mn, J. Phys. F **9**, 2439 (1979).

[47] N. P. Aley and K. O'Grady, Compositional dependence of antiferromagnetic anisotropy in IrMn/CoFe exchange bias systems, J. Appl. Phys. **109**, 07D719 (2011).

[48] J. A. Mydosh, Spin glasses: Redux: An updated experimental/materials survey, Rep. Prog. Phys. **78**, 052501 (2015).

[49] J. M. Rojo, J. L. Mesa, L. Lezama, J. L. Pizarro, M. I. Arriortua, J. Rodriguez Fernandez, G. E. Barberis, and T. Rojo, Spin-glass behavior in a three-dimensional antiferromagnet ordered phase: Magnetic structure of Co$_2$(OH)(Po$_4$), Phys. Rev. B **66**, 094406 (2002).

[50] S. Chillal, M. Thede, F. J. Litterst, S. N. Gvasaliya, T. A. Shaplygina, S. G. Lushnikov, and A. Zheludev, Microscopic coexistence of antiferromagnetic and spin-glass states, Phys. Rev. B **87**, 220403(R) (2013).

[51] R. Carpenter, A. J. Vick, A. Hirohata, G. Vallejo-Fernandez, and K. O'grady, Effect of grain cutting in exchange biased nanostructures, J. Appl. Phys. **115**, 17B905 (2014).

[52] G. Vallejo-Fernandez, N. P. Aley, J. N. Chapman, and K. O'Grady, Measurement of the attempt frequency in antiferromagnets, Appl. Phys. Lett. **97**, 222505 (2010).

[53] B. Craig, R. Lamberton, A. Johnston, U. Nowak, R. W. Chantrell, and K. O'Grady, A model of the temperature dependence of exchange bias in coupled ferromagnetic/antiferromagnetic bilayers, J. Appl. Phys. **103**, 07C102 (2008).

[54] C. Zener, *Elasticity and Anelasticity of Metals.* (University of Chicago Press, Chicago, 1948).

[55] R. Y. Umetsu, A. Sakuma, and K. Fukamichi, Magnetic anisotropy energy of antiferromagnetic l10-type equiatomic Mn alloys, Appl. Phys. Lett. **89**, 052504 (2006).

[56] R. F. L. Evans, L. Rózsa, S. Jenkins, and U. Atxitia, Temperature scaling of two-ion anisotropy in pure and mixed anisotropy systems, Phys. Rev. B **102**, 020412(R) (2020).